

STARTPAGE

THESIS SUMMARY FOR THE 2022 ISRM ROCHA MEDAL
AWARD

Coupled Experimental and Numerical Investigations on Rock Fracturing and Fragmentation Subject to Impact Loading

Xiaofeng Li

Institute of Rock and Soil Mechanics, Chinese Academy of Sciences
Department of Civil Engineering, Monash University

Hongkong, December, 2020

Attributions

This thesis has been awarded as the [Springer Thesis Award \(2020\)](#), the [Outstanding Doctoral Dissertation of CSRME \(2020\)](#), and the [Outstanding Doctoral Dissertation Award of Chinese Academy of Sciences \(81/6432\)](#). The thesis has resulted in eight journal articles and two conference papers, which are listed as below:

Chapter 4:

Li XF, Li HB, Ju MH. Experimental techniques and dynamic behaviour on Brazilian disc testing of rocks using high-speed digital image correlation analysis. *International Journal of Mechanical Sciences*. 2020 (under review)

Li XF, Li HB, Zhang GK, Ju MH, Zhao J. Rate dependency mechanism of crystalline rocks induced by impacts: Insights from grain-scale fracturing and micro heterogeneity. *International Journal of Impact Engineering*. 2021 (online)

Li XF, Li HB, Zhao J. Dynamic behaviours of rocks: the grain scale fracturing characteristics on strength and fragmentation. In *Proceedings of 6th International Conference on Design and Analysis of Protective Structures, 2017, Melbourne, Australia*.

Chapter 5:

Li XF, Li HB, Zhang QB, Jiang JJ, Zhao J. Dynamic fragmentation of rock material: characteristic size, fragment distribution and pulverization law. *Engineering Fracture Mechanics*, 2018. 199:739–59.

Li XF, Li HB, Zhao J. Research on dynamic behaviours of rock material: rate dependency and pulverization. In *Proceedings of the 3rd International Conference on Rock Dynamics and Applications, 2018, Trondheim, Norway*.

Chapter 6:

Li XF, Li X, Li HB, Zhang QB, Zhao J. Dynamic tensile behaviours of heterogeneous rocks: The grain scale fracturing characteristics on strength and fragmentation. *International Journal of Impact Engineering*, 2018, 118: 98-118.

Chapter 7:

Li XF, Li HB, Zhao J. Transgranular fracturing of crystalline rocks and its influence on rock strengths: insights from a grain-scale continuum-discontinuum approach. *Computer Methods in Applied Mechanics and Engineering*. 2021, 373, 113462.

Li XF, Li HB, Liu LW, Liu YQ, Ju MH, Zhao J. Investigating the crack initiation and propagation mechanism in brittle rocks using grain-based finite-discrete element method. *International Journal of Rock Mechanics and Mining Sciences*, 2020, 127: 104219.

Li XF, Li HB, Zhao J. The role of transgranular capability in grain-based modelling of crystalline rocks. *Computers and Geotechnics*, 2019, 110: 161-183.

Chapter 8:

Li XF, Zhang QB, Li HB, Zhao J. Grain-based discrete element method modelling of multi-scale fracturing in rocks under dynamic loading. *Rock Mechanics and Rock Engineering*, 2018; 51: 3785–3817.

Highlights

1. The rate dependency mechanism and dynamic fragmentation of rocks (Experimental advancements)

- This thesis proposed a newly high-speed digital image correlation method to obtain the microsecond-scale spatiotemporal evolution of the deformation fields in rock under impact loads (Fig. 1);
- The fragmentation analysis method based on image processing technique is developed to obtain the continuous debris distribution of rock from meso scale to macro scale, and a novel energy-based fragmentation model considering the strain energy is presented to uncover the rate-dependent fragmentation size and distribution (Fig. 2);
- The dynamic fracturing of rocks spanning from mineral scale to laboratory scale are characterized, and the strain rate effect mechanism led by the transition from intergranular fracturing to transgranular fracturing is revealed.

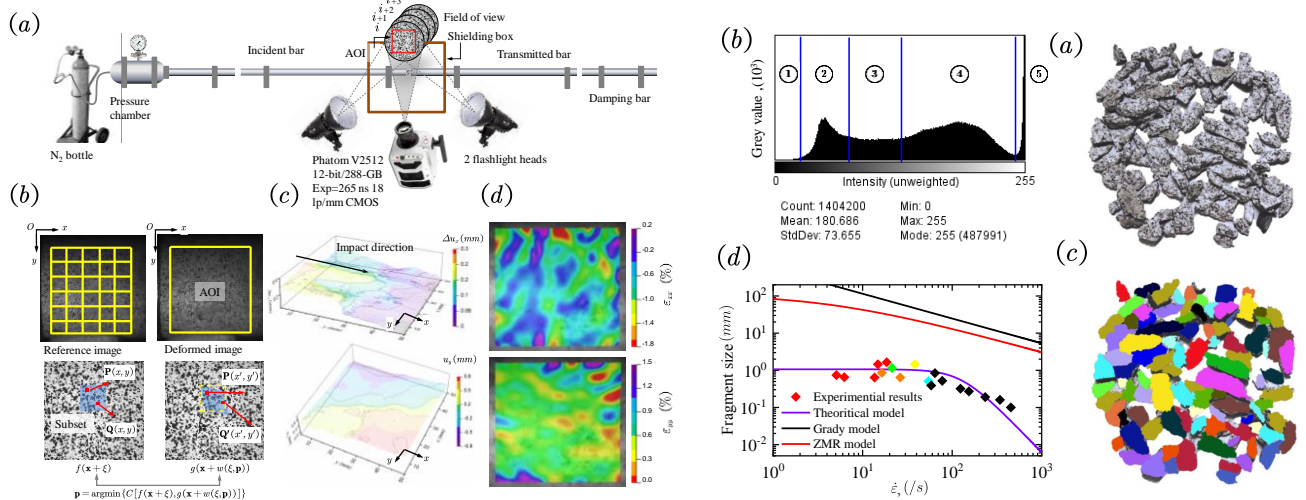


Fig. 1 High-speed DIC method. Fig. 2 Relationship between average fragment size and strain rate.

2. The unified dynamic strength model of fractured rocks (Theoretical advancements)

- The fractured rock model considering the effect of multicrack interaction is proposed, and the normalized dynamic strength model is derived to uncover the micromechanics of the strain rate effect in brittle materials (Fig. 3).
- In cooperation with the database of dynamic tests, the recommended values for the characteristic strain rate and strain rate increase factor of different rocks are obtained. It provides unbiased references to the engineering applications regarding the fact that present investigations or reports are often estimated by trail and error. (Fig. 4).

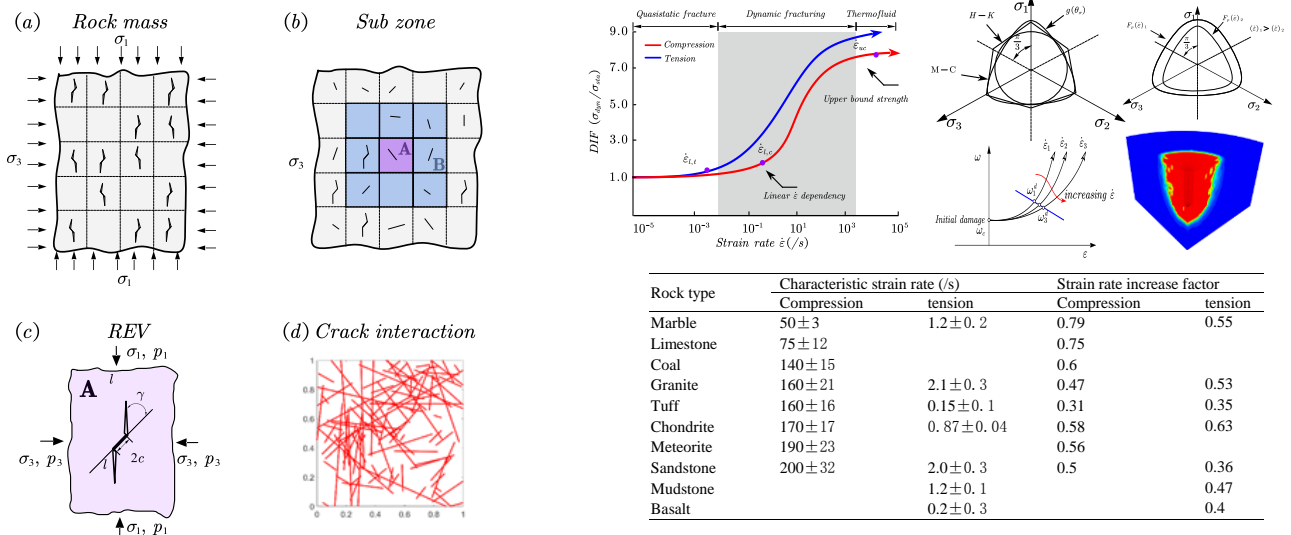


Fig. 3 Randomly multicracked fractured rock model. Fig. 4 The unified dynamic strength model and applications in rock blasting.

3. The grain-scale fracturing and a continuum-discontinuum method (Verification of proposed solution)

- This project offers a novel and reliable open-source multiscale continuum-discontinuum modelling algorithm with

rigorous microstructural characterizations, and provides insights to understand the role of grain-scale fracturing and micro heterogeneity on the rate-dependency and pulverization (Fig. 5).

- The multiscale model is capable of modelling transgranular fracturing, and the nonlinear fracturing model based on the fracture process zone overcomes the shortcoming of the traditional method which is limited to linear elastic fracture mechanics. The transgranular fracturing within minerals reflect the dynamic deformation and fragment characteristics of rocks under dynamic loads at the grain scale (Fig. 6).

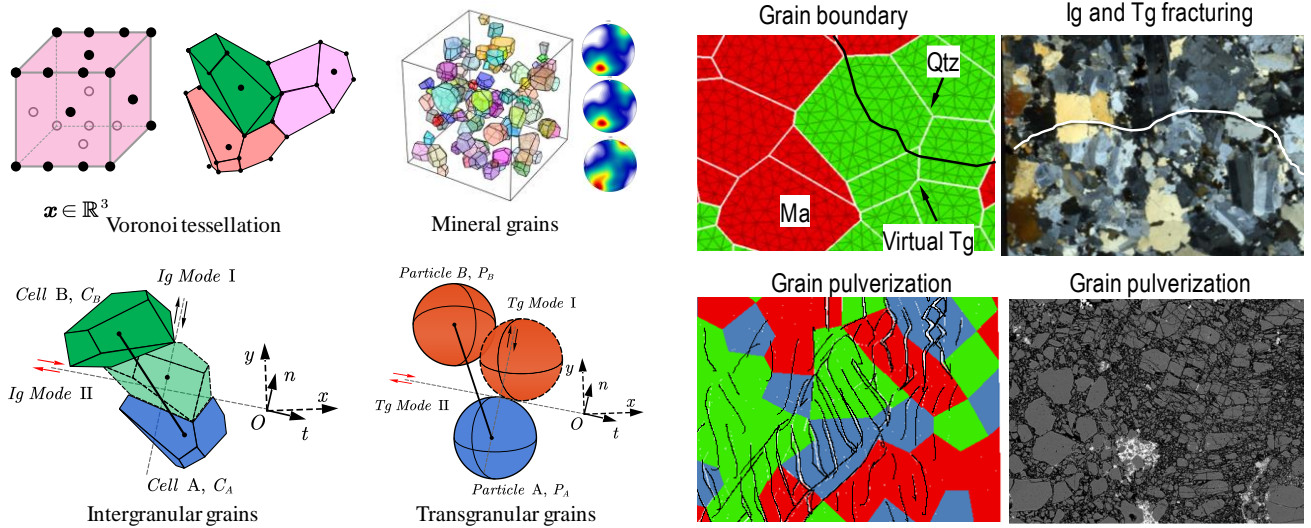


Fig. 5 The schematic diagram of the multiscale continuum-discontinuum model. Fig. 6 Intergranular fracturing and transgranular fracturing within grains.

1. Introduction

1.1 Motivation and objective research

Rock deformation and breakage behaviour under dynamic loading have significant impacts on various engineering problems such as tunnelling (Hajiabdolmajid and Kaiser 2002), earthquake (Aydan 2016), projectile penetration (Heuzé 1990), and exploration drilling for oil, gas and nuclear waste deposits. Rock fragmentation or fault pulverization, consisting of fragments much smaller than the naturally existing minerals of the host rock, has been found near fault cores induced by dynamic slip localisation (Doan and Gary 2009), rockfall (Vagnon et al. 2020), rock bursts in underground excavation (Feng et al. 2017) and blasting (Zhang 2017). This intensively fractured rock indicated that the fragment formation and fracturing generally behaved in strong rate dependency and the energy dissipation or fragment size distribution is significantly different from that of static loading. The dynamic damage process and microscale fracturing of rocks are still challenging to be well understood. Especially by considering the small strain to failure of brittle materials, several uncertain issues, *e.g.*, the improvement of the valid strain rate range, reproducing the micro-damage process under dynamic loading and the instinct micro-fracturing mechanism considering the heterogeneity of rocks, are remaining to be addressed.

The explicit consideration of the actual microheterogeneity of rocks both *in-situ* and in the laboratory is important. Many problems remain to be solved to build the bridge linking the variability of microstructures with the macro dynamic properties which shows significant rate dependency, including (a) what's the actual heterogeneity on the grain scale and how to characterize it in modelling? (b) how to develop the relation between the micro properties and macro behaviours? and (c) what's the reason causes the conversion from intergranular fracturing to transgranular fracturing in solids? Due to the difficulty of reproduction the natural earthquake in the laboratory, the available computational method can be used to model the site-scale modelling will be rather desirable.

1.2 Dissertation structure

Following the introduction [Problem statement], this dissertation is laid as follows:

Chapter 2 [Appreciation of State of the Art] performs the state of the art of rock strength, fracturing and fragmentation due to impacts and the experimental methodology is illustrated in Chapter 3. After that, the rate dependency mechanism of rocks in dynamic tensile splitting, the microsecond-scale deformation fields and rate-dependent fractal surface roughness are investigated in Chapter 4 [Practical advancements]. Chapter 5 [Practical advancements] studies the characteristic size, fragment distribution and pulverization law of rocks under dynamic compression loads. Two typical failure patterns are proposed and a novel energy-based fragment model is carried out to address the pulverization of rocks under high strain rate. A random fractured rock model considering crack interaction is built to explore the mechanism of strain rate in Chapter 6 [Theoretical advancements]. The unified dynamic strength model is derived and the parameters are obtained in cooperation with the database of dynamic tests for different rocks. In Chapter 7 [Numerical advancements], a new open-source multiscale continuum-discontinuum method is developed to explicitly consider the actual microheterogeneity in rocks and Chapter 8 [Verification of proposed solution] validates the effect of heterogeneity on the dynamic fracturing and fragmentation of rocks from mineral scale to laboratory scale. Eventually, the rate-dependency mechanism observed from experiments and the unified dynamic strength model from theory analysis are numerically validated.

2. State of the art of rock strength, fracturing and fragmentation due to impacts

2.1 The strain rate effect

Reliable characterisation on rock mechanical properties under dynamic loading is crucial. The split Hopkinson pressure bar (SHPB) is used in the strain rate range of $10^1 \sim 10^4 \text{ s}^{-1}$, which is generally considered as high strain rate (HSR) (Kolsky 1949; Zhang and Zhao 2014). Previous studies show that the dynamic increasing factor (DIF) has a nonlinear increase in the strain rate at the full scope for quasi-brittle materials. This change includes a slight linear enhancement at low strain rate, rapid increase at HSR and rate independence at ultra-high strain rate. The dynamic fracturing transits from a single fractured \rightarrow fragmented \rightarrow pulverized, and then turns into the thermal fluid when the strain rate exceeds the upper threshold of Hugoniot elastic limit (HEL). All empirical laws for quasi-brittle materials are illustrated in Table 2.1. However, the existing laws are not rigorous enough for fully describing the dynamic behaviours, *e.g.*, the Olsson model has the advantages of fewer parameters but poor ability to characterize the intermediate strain rate behaviours; in Kimberly's model, the rate increase factor is limited to 2/3 which violates the experimental results by different experimental methods as listed in Table 2.2.

Table 2.1 Reviewed empirical strain rate model for quasi-brittle material

References	Material	Strain rate semi empirical equation
Liu, 1980	Rock	$\sigma_{dyn} = \sigma_{sta} e^{c\dot{\epsilon}}$
Grady and Lipkin, 1980	Rock	$\sigma_{dyn} = \left(\frac{2bE^2}{C_g}\right)^{\frac{1}{3}} \dot{\epsilon}^{\frac{1}{3}}$
Lankford,1981	Rock	$\sigma_{dyn} \propto \begin{cases} \dot{\epsilon}^{\frac{1}{n_c+1}} & \dot{\epsilon} \leq \dot{\epsilon}_c \\ \dot{\epsilon}^{\frac{1}{n}} & \dot{\epsilon} > \dot{\epsilon}_c \end{cases}$
Olsson, 1991	Rock	$\sigma_{dyn} = \sigma_{sta} a \dot{\epsilon}^n$
Comite´ Euro-International du Be´ton, 1993	Concrete	$\sigma_{dyn} = \begin{cases} \sigma_{sta} \left(\frac{\dot{\epsilon}}{\dot{\epsilon}_s}\right)^{A\alpha} & \dot{\epsilon}_s < \dot{\epsilon} \leq 30 \text{ s}^{-1} \\ \sigma_{sta} \gamma \left(\frac{\dot{\epsilon}}{\dot{\epsilon}_s}\right)^{0.33} & \dot{\epsilon} > 30 \text{ s}^{-1} \end{cases}$
Malvar and Crawford, 1998	Concrete	$\sigma_{dyn} = \begin{cases} \sigma_{sta} \left(\frac{\dot{\epsilon}}{\dot{\epsilon}_s}\right)^\alpha & \dot{\epsilon}_s < \dot{\epsilon} \leq 1 \text{ s}^{-1} \\ \sigma_{sta} \gamma \left(\frac{\dot{\epsilon}}{\dot{\epsilon}_s}\right)^{0.33} & \dot{\epsilon} > 1 \text{ s}^{-1} \end{cases}$
Johnson et al, 2003	Concrete	$\sigma_{dyn} = \sigma_{sta} (1 + C \ln \dot{\epsilon}^*)$
Zhou and Hao, 2008	Concrete-like material	$\sigma_{dyn} = \begin{cases} \sigma_{sta} (a + b \log(\dot{\epsilon})) & 10^{-4}/s < \dot{\epsilon} \leq 1 \text{ s} \\ \sigma_{sta} (a + c \log(\dot{\epsilon})) & \dot{\epsilon} > 1 \text{ s}^{-1} \end{cases}$
Kimberley et al, 2013	Rock	$\sigma_{dyn} = \sigma_{sta} + \sigma_{sta} \left(\frac{\dot{\epsilon}}{\dot{\epsilon}_s}\right)^{2/3}$
Present study	Rock	$\sigma_{dyn} = \sigma_{sta} + \sigma_{sta} \left(\frac{\dot{\epsilon}}{\dot{\epsilon}_s}\right)^\beta$

Table 2.2 Experimental results of the strain rate effect of brittle materials

Materials	Methodology	Rate increase factor	References
Arkansas Novaculite	Plate impact	1/3	Grady and Kipp, 1979
Quartz Monzonite	SHPB test	1/3	Birkimer 1970
Westerly Granite	SHPB test	1/3	Lipkin
Solenhofen Limestone	SHPB test	0.05	Lipkin et al. 1979
Oakhall Limestone	SHPB test	0.19	Lipkin
Oil Shale	Taylor plate Electromagnetic shock	0.25	Grady and Hollenbach, 1979
Concrete	SHPB test	1/3	Lipkin and Jones ,1979 Birkimer 1970

2.2 State of the art of rock dynamic fragmentation

Shock penetration and dynamic fragmentation of brittle materials cover a wide range of areas including defense and shielding in military use, rockfall, planetary and space sciences, mining and rock fragmentation in understanding faulting. The research on accurate prediction of the fragment size with respect to loading rate continues to be an active field for quasi-brittle materials such as rock, concrete and ceramic by means of theoretical analysis (Naimark et al. 2017), computational simulation (Cereceda et al. 2017) and experimental tests (Dehkhoda and Hood 2013).

From an energy conservation perspective, the shock wave converts the kinetic energy of the projectile into the fracture energy for generating new fracture surfaces (Grady 1982; Glenn and Chudnovsky 1986), residual kinetic energy of flying fragments (Cintala et al. 1999), acoustic emission and dissipated thermal energy (Yew and Taylor 1994). (Grady 1982) used the energy equilibrium that the local kinetic energy of the solid body is consumed for the creation of new fragment surfaces to predict the average fragment size. Considering the strain energy acting as a dominancy dissipation for fragmentation at lower strain rate, (Glenn and Chudnovsky 1986) added the strain energy

term to the energy conservation equation and the predicted average fragment size agrees well with the experiment results in the full strain rate range. Other modified models on the basis of energy equilibrium, including Yew and Taylor model (Yew and Taylor 1994), Miller model (Miller et al. 1999) and YTGC model, are developed to emphasize the partial energy transform among the potential energy of elastic deformation, local kinetic energy and surface energy (see Table 2.3). At lower strain rate, the macroscopic rupture occurs via through-going fractures, whereas the high strain rate loading leads to pervasive and coalesced fractures, which eventually pulverizes the specimen into intensive fragments. The mechanism underlying the catastrophic fragmentation is the improvement of the probability of defects activation with considerable energy driving in extremely short duration.

2.3 Overview of grain-based modelling algorithm

The explicit consideration of the actual microheterogeneity of rock in numerical modelling is important. The continuous methods having abilities for rupturing modelling, such as FEM with mesh adaptation capability, XFEM, meshfree, phase field and FDEM are advantageous for reproducing the fracturing process of rocks. As an alternative to the continuous method, the multiscale discontinuous method to study the mechanical characteristics of rocks directly on grain scale has developed rapidly. The grain-based method (GbM) contains (a) square-based grain method (SbGM), (b) block-based grain method (BbGM) and (c) particle-based grain method (PbGM) according to the mineral morphology. The SbGM regards the damage or plasticity indicator of the grid as the fracture and fails to reveal the influence of contact heterogeneity on crack initiation and propagation. In BbGM, crystals are modelled as deformable polygonal blocks to characterize the anisotropy of minerals and virtual contacts between blocks can simulate real separation and sliding between minerals (Kim et al. 2013). Although the above method can better simulate the grain structure of rocks, it has the disadvantages of (a) complicated contact discrimination, (b) low computation efficiency, and (c) failure to simulate the fracturing behaviour within the crystals. The particles filling in minerals as computational nodal points allow for transgranular and intergranular failure in the process of rock fracturing using multiscale fracturing models. However, due to the influence of particle morphology, PbGM has limited constraints on grain rotation, which results in (a) low strength ratio; (b) low macroscopic friction angle and (c) approximately linear confining pressure effect in the simulation of rock materials (Cho et al. 2007). The polygonal mineral grains with Voronoi tessellations and the mGbM based on the actual distribution of grains using digital image processing technique were proposed (Li et al. 2018). The mGbM method inherits the advantage of BbGM in characterization of actual mineral morphology and the advantage of PbGM in high computation efficiency as well as the ability to model transgranular fracturing. The reasonability of mGbM and its application in rock materials led by quasi-static and dynamic fracturing are discussed in detail in Table 2.4.

Table 2.3 Review of the dynamic fragment model

Method	Average fragment size	Comments	Refs.
Grady model	$s_{Grady} = \left(\frac{\sqrt{12} K_{IC}}{\rho c \dot{\epsilon}} \right)^{2/3}$	a. Energy conservation b. Ignoring strain energy	Grady, 1982
Glenn and Chudnovsky model	$s_{GC} = 2\sqrt{\frac{\alpha}{3}} \sinh \frac{\phi}{3} \phi = \sinh^{-1} \left(\beta \left(\frac{3}{\alpha} \right)^{3/2} \right)$	a. Energy conservation b. Considering strain energy	Glen and Chudnovsky, 1986
Yew and Taylor model	$s_{YT} = \left(\frac{\sqrt{3} K_{IC}}{\rho c \dot{\epsilon}} \right)^{2/3} \quad s_{YT} = \left(\frac{\sqrt{3} K_{IC}}{\rho c \dot{\epsilon}} \right)^{2/3}$	a. Thermodynamic equilibrium	Yew and Taylor, 1994
Miller model	$s_{Miller} = \left(\frac{\sqrt{24} K_{IC}}{\rho c \dot{\epsilon}} \right)^{2/3}$	a. Energy conservation b. Ignoring strain energy	Miller et al, 1999
Zhou model	$s_{ZMR} = \frac{4.5 s_0}{1 + 4.5 (\dot{\epsilon}/\dot{\epsilon}_0)^{2/3}}$	a. Numerical fitting	Zhou et al, 2006
Zhou model	$s_{Zhou} = 4.5 s_0 \left[1 + 0.77 \left(\frac{\dot{\epsilon}}{\dot{\epsilon}_0} \right)^{1/4} + 5.4 \left(\frac{\dot{\epsilon}}{\dot{\epsilon}_0} \right)^{3/4} \right]^{-1}$	a. Numerical fitting	Zhou et al, 2006
YTGC model	$s_{YTGC} = \left(\frac{2K_{IC}}{\rho \sigma_0 \dot{\epsilon}} \right)^{1/2}$	a. Energy conservation b. Ignoring kinetic energy	Stránský, 2010
Levy and Molinari model	$s_{LM} = \frac{3t_0 C_{eff}}{1 + 4.5 (Et_0/\mu_{init})^{2/3} \dot{\epsilon}^{2/3}}$	a. Considering existed defect b. Numerical fitting	Levy and Molinari, 2010

Table 2.4 Overview of grain-based modelling of geomaterials

Application	Method	Grain methodology	Grain crushing ability	Results	Advantages/disadvantages	Literature
Rate dependence of concrete	Discrete element approach, irregular lattice model with rigid-body-spring network	Polygon-based grain	Rigid grains	Rate dependence is a behaviour of viscosity of concrete	(a) Grain element is rigid (b) Two-dimensional model (c) Stochastic grain distribution	Kim and Lim, 2011
Dynamic behaviours of RC structure				Load-carrying capacity of RC concrete		Kim et al. 2013
Mixed mode fracture test and plate impact					(a) 3D grain-based model	Hwang and Kim, 2017 ; Rasmussen et al. 2018
Actual material heterogeneity	FDEM; X-ray MicroCT	Triangle-based method, actual grain shape	Deformable grains with intergranular capability	Actual micro heterogeneity is reproduced and micro parameters are calibrated by micro indentation	(a) Actual grain distribution (b) Grain crushing is available (c) Two-dimensional model;(d) mesh dependent	Mahabadi et al. 2012a ; Mahabadi et al. 2014
Brazilian disc test	FDEM; X-ray MicroCT	Triangle-based method, actual grain shape	Deformable grains	Micro heterogeneity and microstructures on the tensile behaviours	(a) Two-dimensional model (b) Mesh size influences actual fracturing	Mahabadi et al. 2012b ;
Uniaxial compression test; Brazilian disc test, Wedge chipping	FDM; FLAC ^{2D}	Square-based method, stochastic grain distribution	Deformable grains, fracturing is represented by plasticity	Heterogeneity and mineral properties on UCS and BTS	(a) No grain boundaries (b) Two-dimensional model	Villeneuve et al. 2012
Uniaxial compression test	FEM; RFPA ^{2D}	Square-based method, random grain shape	Element degradation in grains	Failure process of granite	(a) Stochastic grain distribution (b) No grain boundary (c) Damage-based grain crushing	Li et al. 2003 ; Liu et al. 2004
				Thermal treatment on grain crushing		Lu et al. 2015
Brazilian disc test	FDM;FLAC ^{2D}	Square-based method, image-based grain modelling Actual 3D CT method	Element plasticity	Rock heterogeneity on rock tensile behaviours	(a) Digital image-based modelling (b) Intergranular cracking is ignorable	Chen et al. 2004
					(a) Three-dimensional model	Chen et al. 2007
Dynamic loading	Meshfree; SPH	Node-based method	Damage degradation	Dynamic failure and strain rate mechanism	(a) Stochastic grain distribution (b) Phenomenological failure	Ma et al. 2014

Uniaxial compression test, Brazilian disc test; fracturing test	DEM; UDEC-grain model	Voronoi tessellation	Elastic minerals, grain crushing is unavailable	Stress heterogeneity induces brittle extensile fracturing of rocks	(a) More realistic grain morphology (b) Grain is unbreakable (c) 2D model	Lan et al. 2010; Nicksiar and Martin, 2013; Chen and Konietzky, 2014; Chen et al. 2016; Gui et al. 2016; Park et al. 2017 Tan et al. 2016
Brazilian disc test	DEM; UDEC-grain model	Voronoi tessellation	Element plasticity	The role of grain heterogeneity on rock tensile strength	(a) Mineralogy is revealed (b) Grain can fail (c) Digital image-based model	
Uniaxial compression test, Brazilian disc test	DEM; UDEC-grain model	Dual-layer model, Voronoi tessellation of mineral grains, triangle-based element intragrain	Grain crushable	The role of grain crushing on rock static fracturing	(a) Two-dimensional grain model (b) Grain parameters are difficult to obtain (c) High computation consumption	Kazerani and Zhao, 2010; Gao et al. 2016
Uniaxial compression test	FDEM, Irazu-grain	Polygon-based grain	Grain crushable		(a) Grain can be broken (b) FDEM increases computation efficiency (c) Commercial code	Abdelaziz et al. 2018
Compression test, Brazilian disc test	FDEM, GB-FDEM	Actual grain shape	Grain crushable	Inter/intra behaviours on crack fracturing of rocks	(a) Realistic reproduction of grain morphology (b) Grain is crushable (c) FDEM increases computation efficiency	Li et al. 2018a and b
Uniaxial compression test, Brazilian disc test	DEM. 3DEC-trigon model	Trigon-shaped grains	Elastic minerals	Microfracturing is achieved in 3D DEM modelling	(a) Grain is unbreakable (b) Grain shape is overlooked (c) Mineralogy is overlooked	Gao and Stead, 2014
Uniaxial compression test	DEM, UDEC	Voronoi-shaped and Trigon-shaped grains	Elastic minerals	Uncertainty induced by grain boundary modes		Mayer and Stead, 2017
Uniaxial compression test	NMM	Voronoi tessellation				Liu et al. 2018
Uniaxial compression test	DEM; 3DEC-Voronoi	Voronoi tessellation	Elastic minerals, material is homogenous	Fabric-guided micro fracturing	(a) 3D grain model (b) No grain crushing	Ghazvinian et al. 2014

Compression and tension test	DEM; 3PDEM	Polygon-based grains	Elastic minerals	Grain structure on rock strengths	(a) 3D grain model (b) No grain crushing	Li et al. 2016a ; Li et al. 2017
Uniaxial compression test	DEM; 3DEC-Voronoi	Dual-layer Voronoi grains	Element plasticity, grain is crushable		(a) 3D stochastic grain distribution	Wang and Cai, 2018
Compression test, direct shear test	DEM; PFC-grain model	Particle clustered grain	Dual-layer modelling, grain crushing is allowed	Confinement mechanism is highly related to grain-scale fracturing	(a) Grain crushing is available (b) Stochastic grain distribution (c) Parameter calibration is difficult (d) Smooth joint model is used for grain boundary	Bahrani et al. 2014 ; Bewick et al. 2014a and b ; Hofmann et al. 2015a and b ; Bahrani and Kaiser, 2016 ; Peng et al. 2017a ; Peng et al. 2017b ; Bahrani and Kaiser, 2017 ; Peng et al. 2018 ; Liu et al. 2018
SHPB test	DEM; multiscale DEM	Actual grain shape, dual-layer grains, particle-based method	Grain crushable	Strain rate mechanism and microfracturing transition	(a) Grain crushing is available (b) Realistic reproduction of grain shapes	Li et al. 2018c and d

3. Experimental methodology

3.1 Sample preparation

Granitic rock sample with high heterogeneity was used to study the dynamic behaviour under impact loads in this thesis. The main mineral contents are quartz (Qtz), soda feldspar (Soda Fsp), plagioclase, mica (ma) and a few other minerals. The content ratio of different minerals is estimated from the thin section and EBSD images in Fig. 3.1a and b (see details in Table 3.1). Image analysis indicates the average grain sizes of Qtz, Fsp and ma are 1.88 mm, 2.64 mm and 0.85 mm, respectively. The orientation distribution of grain boundaries in the granite sample is depicted in Fig. 3.1c.

3.2 Kolsky bar impacts and high-speed digital image correlation

Dynamic experiments are conducted with the Kolsky bar as shown in Fig. 3.2. The setup is consisted of loading system, high speed camera system and strain measurement system. The loading system includes the incident bar, transmitted bar and the striker. The high speed camera and conventional strain gauges are used to capture deformation signals across the sample. The strain, strain rate and stress of the sample are (Zhou et al. 2012)

$$\begin{aligned}\varepsilon_s &= \frac{C_b}{l_s} \int_0^{t_0} (\varepsilon_{in} - \varepsilon_{re} - \varepsilon_{tr}) dt \\ \dot{\varepsilon}_s &= \frac{C_b}{l_s} (\varepsilon_{in} - \varepsilon_{re} - \varepsilon_{tr}) \\ \sigma_s &= \frac{E_b A_b}{2A_s} (\varepsilon_{in} + \varepsilon_{re} + \varepsilon_{tr})\end{aligned}\quad (3.1)$$

The principle of DIC is computing the full-field displacement and strain based on the comparison of two images at different moments. The cross-correlation function \mathcal{G}_{cc} is defined as the two-dimensional spatial convolution of the intensity values of the two images as

$$\mathcal{G}_{cc} = \sum_{i=1}^m \sum_{j=1}^m I(x_i, y_j) I^*(x_i^*, y_j^*) \quad (3.2)$$

where m is the pixel number of the subset. $I(x_i, y_j)$ and $I^*(x_i^*, y_j^*)$ are the intensity values of images before and after deformation. The strains are determined by

$$\begin{aligned}\varepsilon_{xx} &= \frac{\partial u}{\partial x} + \frac{1}{2} \left[\left(\frac{\partial u}{\partial x} \right)^2 + \left(\frac{\partial v}{\partial x} \right)^2 \right] \\ \varepsilon_{yy} &= \frac{\partial v}{\partial y} + \frac{1}{2} \left[\left(\frac{\partial u}{\partial y} \right)^2 + \left(\frac{\partial v}{\partial y} \right)^2 \right] \\ \varepsilon_{xy} &= \frac{1}{2} \left(\frac{\partial u}{\partial y} + \frac{\partial v}{\partial x} \right) + \frac{1}{2} \left(\frac{\partial u}{\partial x} \frac{\partial u}{\partial y} + \frac{\partial v}{\partial x} \frac{\partial v}{\partial y} \right)\end{aligned}\quad (3.3)$$

The rock undergoes large strain, large displacement, high strain rate and huge background noise under impact loads. The cross-correlation function ZNSSD with strong anti-interference ability is proposed for dynamic loading tests, the correlation coefficient of ZNSSD will not change even when the light intensity in ROI changes

$$\mathcal{G}_{ZNSSD} = \sum_{i=-m}^m \sum_{j=-m}^m \left[\frac{I(x_i, y_j) - I_m}{\Delta I} - \frac{I^*(x_i^*, y_j^*) - I_m^*}{\Delta I^*} \right]^2 \quad (3.4)$$

3.3 Fragment analysis algorithm based on image processing

Fragment size analysis was carried out by a combination of sieving method and image processing technique for the fragmented rocks. Taking advantage of the ability to measure the size of each fragment by using the image processing technique, the digital grain size analysis based on the edge detection method is proposed. This technique contains two main steps: (i) gray-scale thresholding to create a binary image and (ii) watershed segmentation to detect edges on the binary image to identify individual debris. A segmentation algorithm written in MATLAB is implemented to identify debris in each sieving regime over high-resolution images with a size of 3024×3024 pixels. Each photograph samples a 10×10 cm area, and the image spatial resolution is approximately 0.03 mm per pixel (in Fig. 3.3).

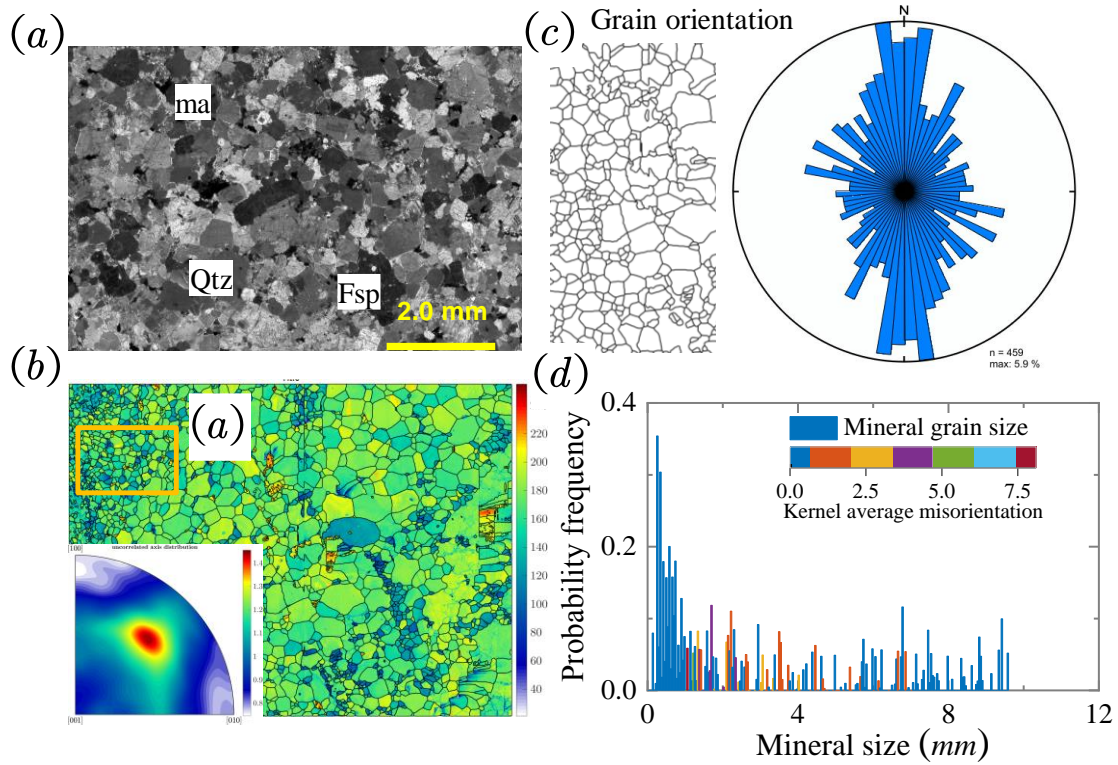


Fig. 3.1 (a) Thin section images of the granite sample.(b) Rock digitization of the EBSD grain orientation map, (c) the orientation distribution of the grain boundaries, (d) the grain size distribution.

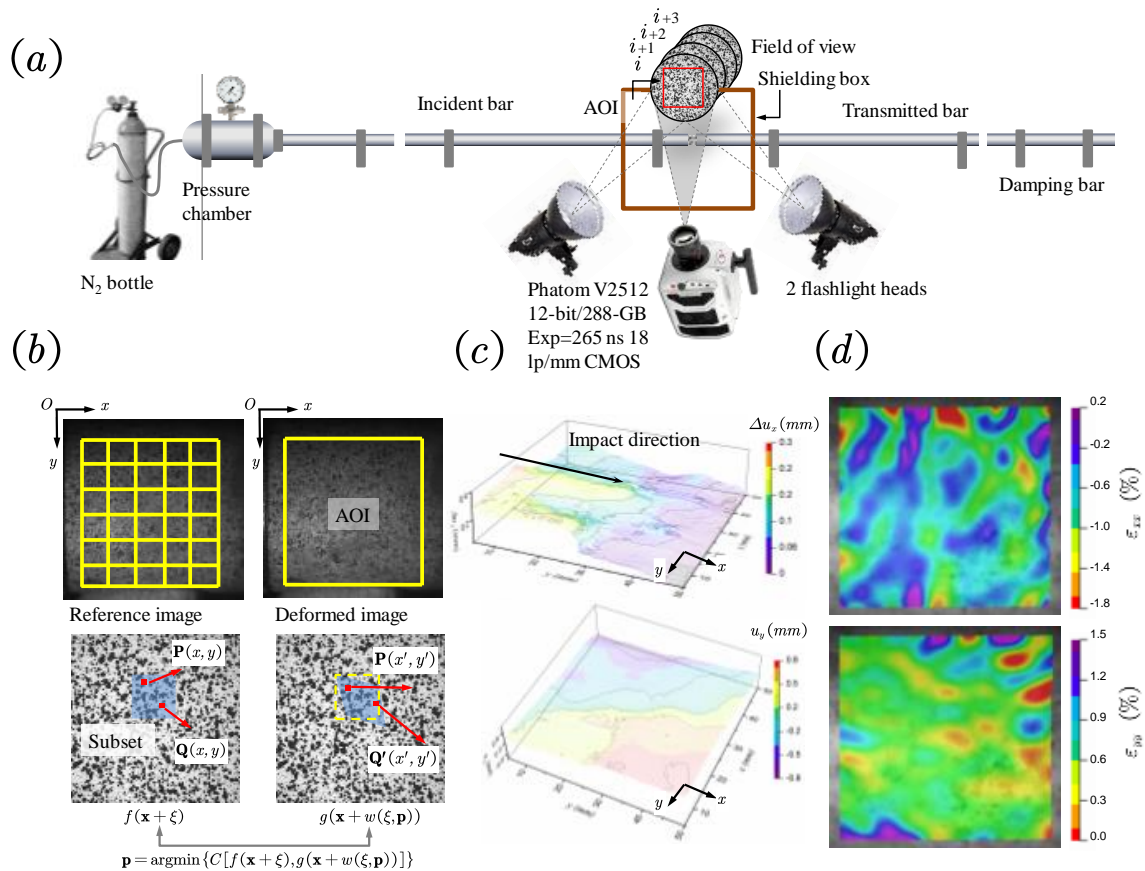


Fig. 3.2 Digital image correlation analysis in high speed impact test.

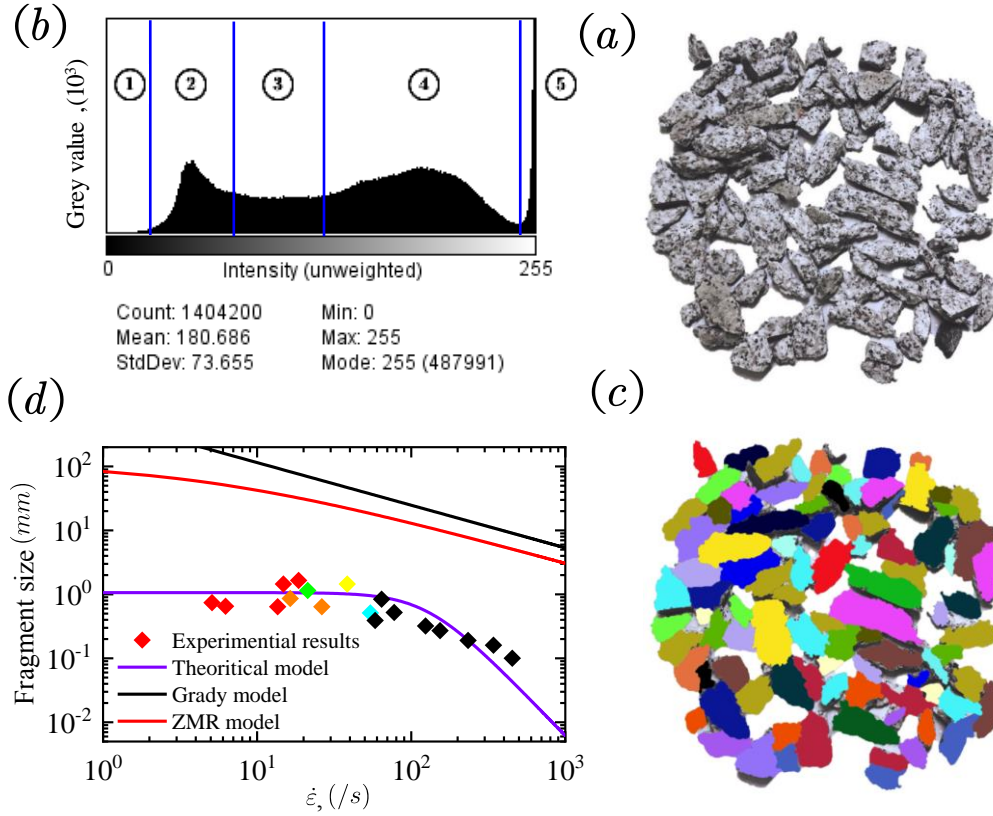


Fig. 3.3 Flow chart of proposed image processing method for fragment size detection.

Table 3.1 Mineral composition and grain size of granites

Minerals	Chemistry ingredient	Content%	Minimum size(mm)	Maximum size(mm)	Average size(mm)
Quartz	SiO ₂	32.7	0.86	2.45	1.88
Feldspar	KAlSi ₃ O ₈	52.6	1.46	4.54	2.64
Mica	K ₃ Si ₃ O ₁₀	14.3	0.28	1.54	0.85
others		0.4	0.08	0.45	0.34

4. Rate dependency mechanism of heterogenous rocks induced by tensile splitting

4.1 Microsecond-scale spatial displacement and strain fields

Digital Image Correlation (DIC) has been proven as an effective method to determine the dynamic fracturing process of rocks. The tip of the discontinuity propagates to the ends of the sample and the maximum tensile strain is approximated 1.0% when the stress reaches its peak value (Fig. 4.1). The crack opening displacement (COD) of seven virtual gauges located on the centerline is presented in Fig. 4.2 a. From the results estimated by the naked eye, it is hard to precisely capture the crack tips and the crack velocity is underestimated. The DIC method provides the real-time change of the crack velocity as well as the propagation direction. The value of the crack velocity experimentally determined by DIC is in the range from 200 m/s to 600 m/s (Fig. 4.2).

The peak strain rate coincides with $0.9\sigma_p$, which is identified as the crack initiation moment from the profile of tensile strain exceeding the threshold of 0.4% (in Fig. 4.3). The average value of ϵ_{yy} corresponding to crack initiation is 0.38%. That value of boundary failure is 1.0% in post-peak (Fig. 4.4), and after that moment, the strain field is dramatically distributed because of the displacement discontinuity (Fig. 4.5). The strain rate in this experiment is identified as a constant state on the history curve of strain rate with a value of 5.1/s.

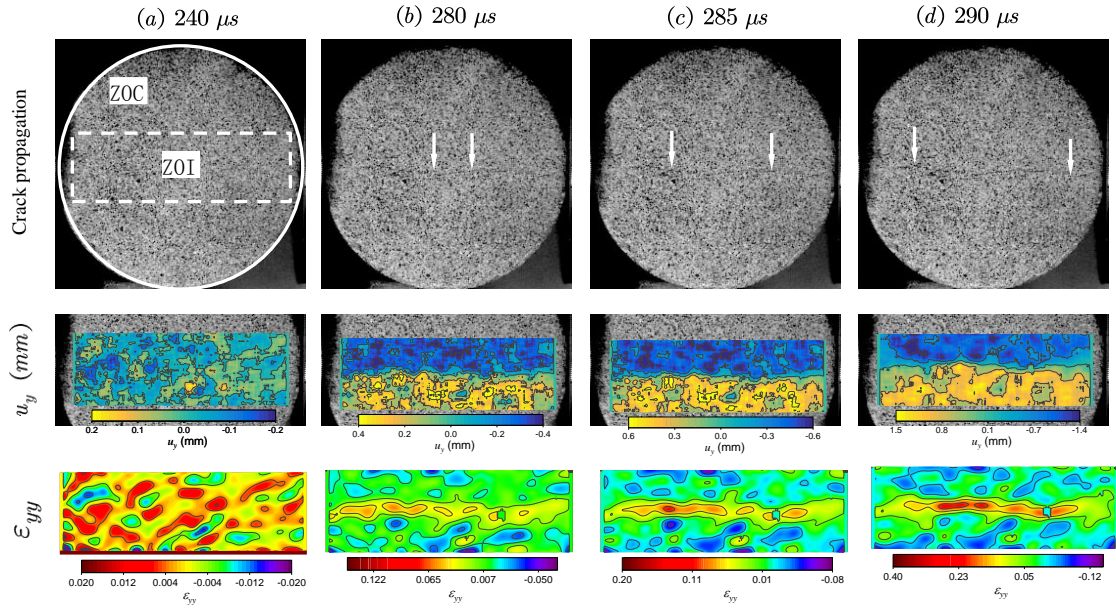


Fig. 4.1 Fracturing sequence, vertical displacement and strain recorded by high speed camera for rock at impact velocity $v=5.6$ m/s.

Table 4.1 Brazilian disc experimental results of granite

Sample No.	$\dot{\epsilon}_{sg}/s$	σ_t MPa	W_{ab} J	E_k J	E_k/W_{ab} %	$G_c J/cm^2$	s_{ave} mm	Boundary condition
GBs-0	1e-5	11.2	—	—	—	—	12.4	Intact
GB-1	6.24	15.4	0.72	0.24	33.3	2.4	0.6	Intact
GB-2	5.1	14.5	4.7	0.78	16.6	19.6	0.74	Intact
GB-3	13.6	16.3	6.8	1.7	25.0	25.5	0.54	Split, conical failure
GB-4	16.4	29.2	24.56	9.8	41.3	73.8	0.86	Split, conical failure
GB-5	26.3	23.4	26.5	7.7	39.9	94.0	0.64	Split, type I
GB-6	14.8	19.7	27.1	11.2	29.1	79.5	1.45	Right end failure
GB-7	18.6	23.3	14.6	4.5	30.8	50.5	1.65	Split, fragmented
GB-8	21.3	31.0	29.4	11.2	38.1	91.0	1.15	Split, crack branch
GB-9	54.3	22.2	34.6	13.2	38.1	91.0	0.51	Fragmented
GB-10	58.4	22.1	41.3	14.6	35.3	117.0	0.23	Split, crack branch
GB-11	64.3	18.6	65.4	15.3	23.4	250.5	0.84	Split, conical failure
GB-12	77.6	24.6	84.3	21.3	25.3	315.0	0.52	Left end failure
GB-13	38.5	18.4	106.4	24.3	22.8	436.5	1.45	Left end fragmented

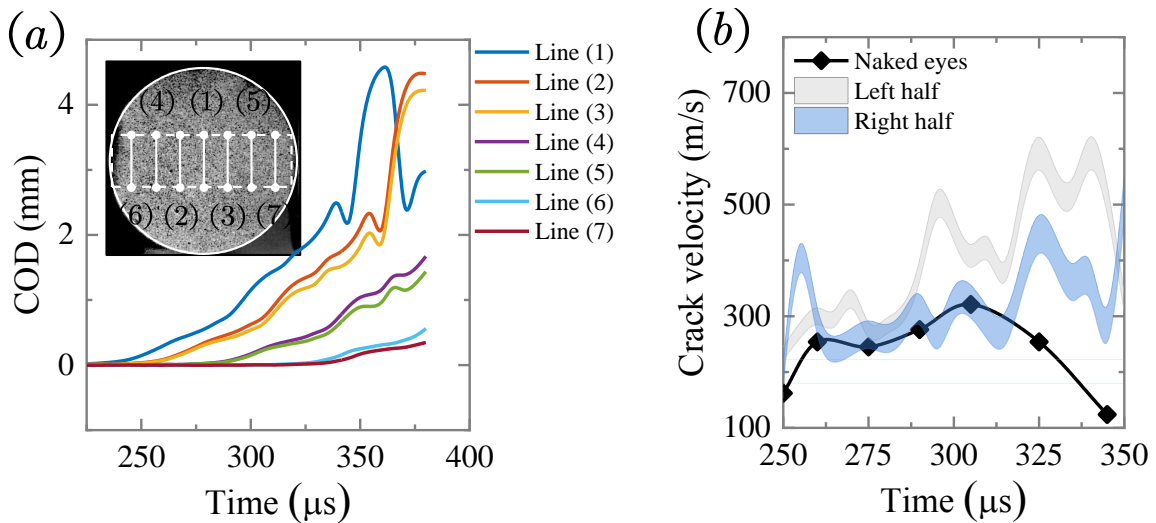


Fig. 4.2 (a) The location of the virtual gauges and COD as a function of time, (b) the comparison of crack velocity computed from DIC, strain gauge and visual method.

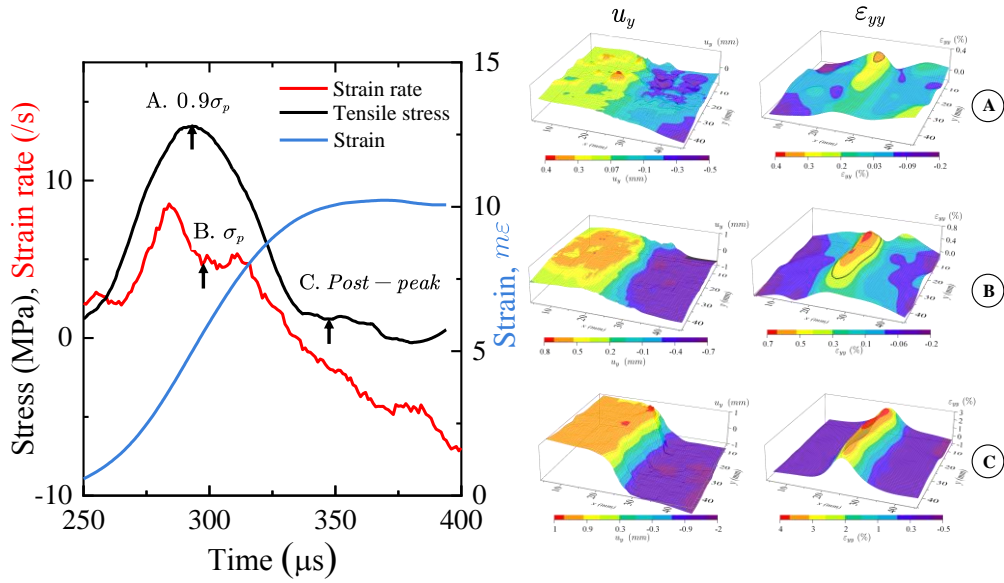


Fig. 4.3 History curves of stress, strain rate and strains on a representative sample and the profiles of displacement and strain fields in y direction at different stress levels.

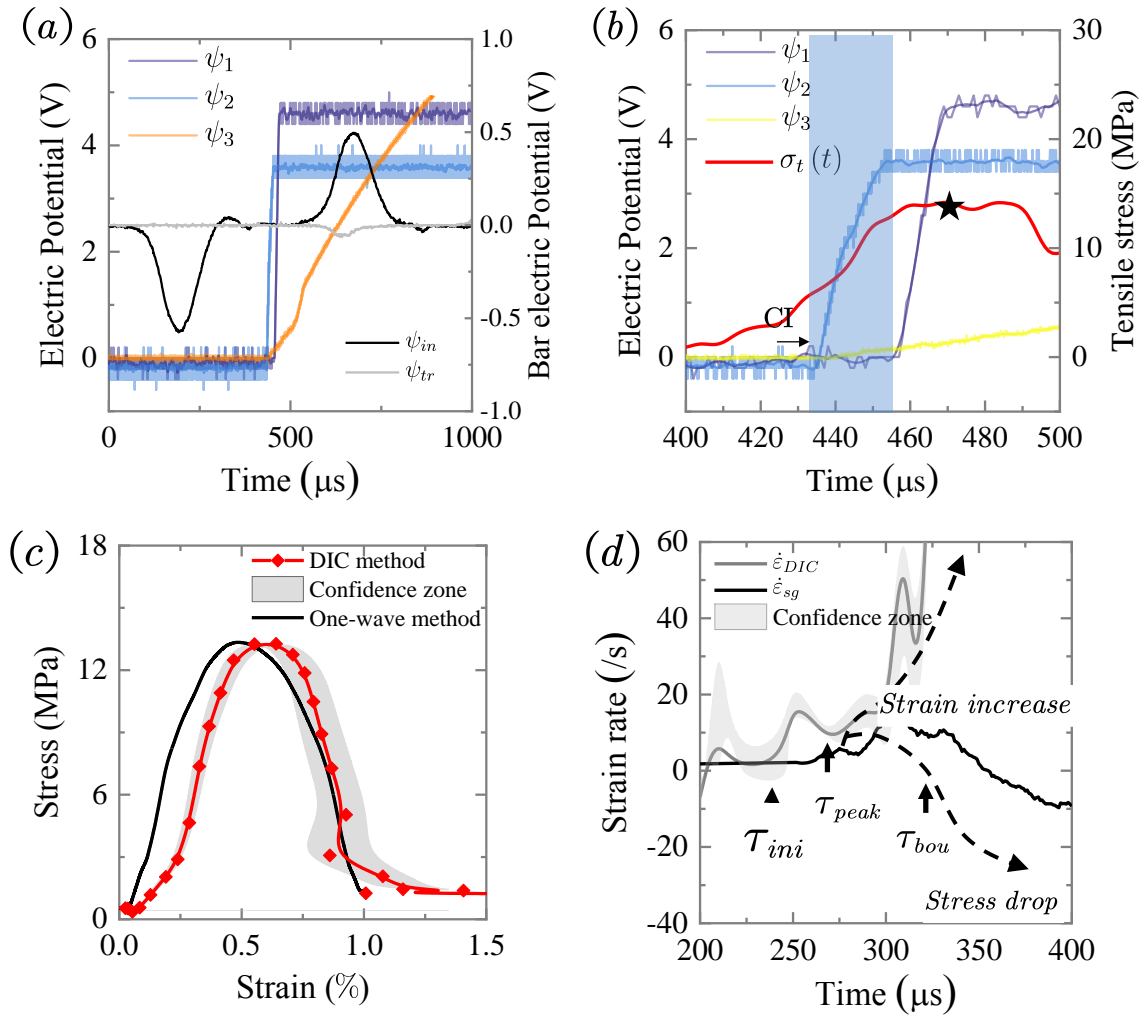


Fig. 4.4 (a) Dynamic results of the sample GB-1, and (b) history of tensile stress. (c) The stress-strain curves and (d) strain rates computed by DIC analysis and strain gauge method.

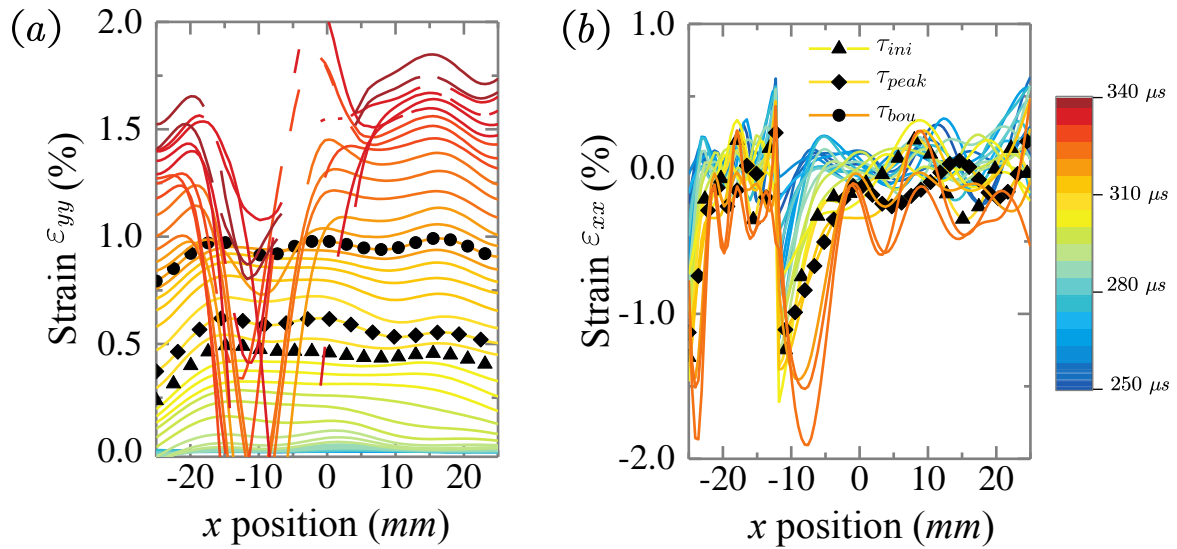


Fig. 4.5 (a) The experimental vertical strain and (b) the horizontal strain on the centerline at different moments.

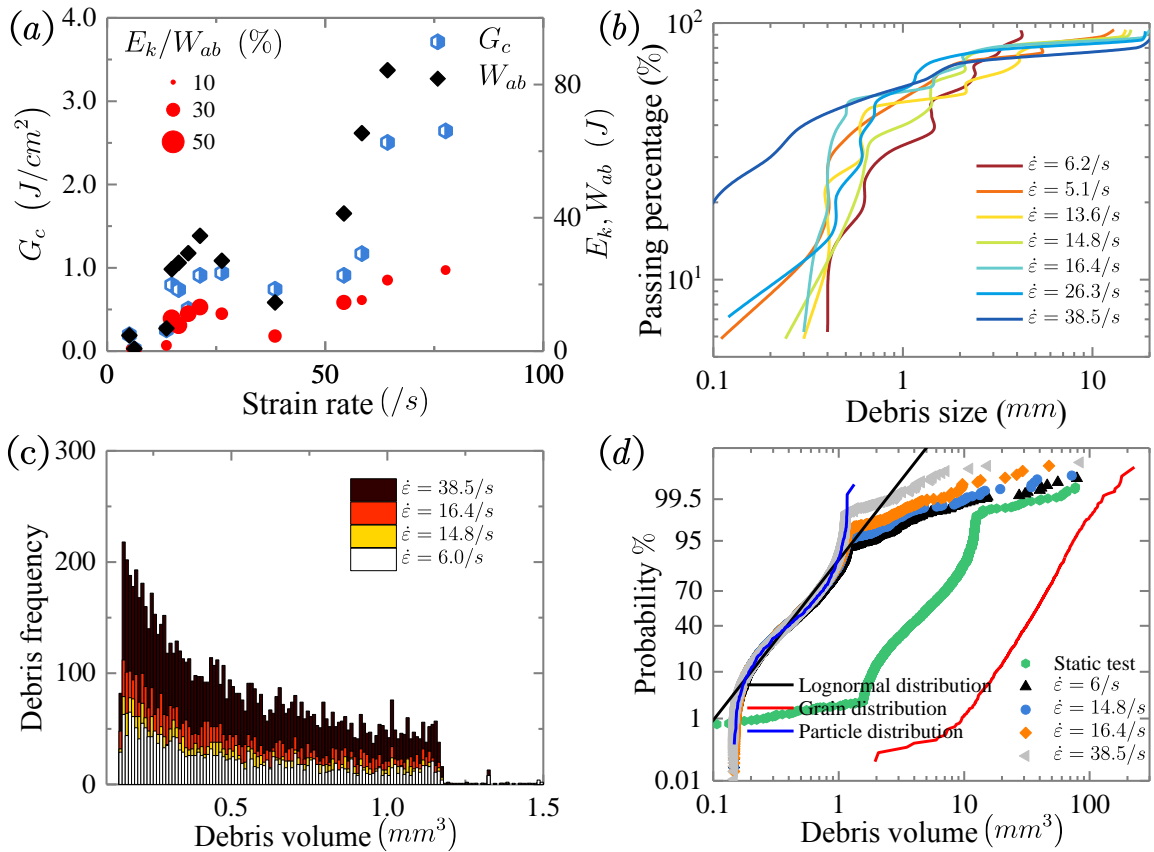


Fig. 4.6 (a) The dissipated energy, residual kinetic energy and fracture energy, (b) the fragment size distribution of samples as a function of strain rate. (c) The histograms of debris volume at different strain rates, (d) cumulative distributions of fragment size at different strain rates.

4.2 Energy transition and rock fragmentation

The energy efficiency in comminution is much low with regarding to the input energy, which is at an order of less 3% in the formation of new surfaces. Even though in rock blasting, the energy consumed for fragmentation will never exceed 6% (Sanchidrián et al. 2007). In experiments, the kinetic energy is figured out by the high-speed camera as

$$E_k = \sum_{i=1}^n \frac{1}{2} m_i v_i^2 \quad (4.1)$$

where m_i and v_i are the mass and velocity of the i th fragment. In this study, the residual kinetic energy is 1.17 J and the fracture energy is 1775 J/m². Higher strain rate results in more energy dissipated in rock fragmentation, which exhibits an exponential increase from 0.76 J to 106.4 J with respect to the strain rate increasing from 6.24/s to 38.5/s. The formation of debris causes more kinetic energy in comparison with other conventional tests, hence, neglecting kinetic energy remarkably overestimates the fracture energy and leads to higher fracture toughness results. From the cumulative probability distribution as a function of debris volume, the relations between the microcrack distribution, fragment distribution and grain distribution are presented (Fig. 4.6). The microcracks distribution within minerals is the lowest bound of fragments exhibiting grain pulverization less than the grain scale, which are commonly observed in quartzo-feldspathic rocks in strike-slip faults, *e.g.* San Andreas fault in California (Dor et al. 2006), Arima-Takatsuki fault in Japan (Mitchell et al. 2011) and North Anatolian fault in Turkey (Dor et al. 2008). The grain distribution is the upper limitation dominated by microstructures within rocks. From the probability curve, we note that about 97% of the fragments in the static test have a volume less than 20 mm³.

4.3 Surface roughness and fractal dimension

Physical features of the fractured surfaces under static and dynamic tests are examined using Geomagic capture 3D scanner (in Fig. 4.7). The experimental results indicate that the surface roughness is slightly decreased when the loading condition transforms from static to dynamic impact. While, the fractal dimension decreases from 2.18 to 2.03, indicating a flatter surface as the fractal dimension approaches to 2.0. Considering a fracture surface due to the fast crack propagation is fractal in homogeneous materials, the relation between real crack velocity and scale size is

$$v = v_0 \left(\frac{L_0}{d} \right)^{D-1} \quad (4.2)$$

where v_0 is the apparent crack velocity, L_0 the apparent crack length and d is the grain size. The results indicate that the fractal property of fracture surfaces over the grain scale exhibits no much significant rate dependency as reported by (Ravi-Chandar and Knauss 1984). Then the fracture morphology is reduced to a scale less than mineral grains using the SEM images. The influence of strain rate on the fractal dimension is decreased as the magnification increases from 200 times to 4000 times and the fractal dimension decreases to 1.66 for the case of $\dot{\epsilon} = 26.3/s$ at 200 times magnification. The textures remaining the topography of the minerals are regarded as intergranular mode I fracturing that occurs on the grain boundaries of quartz, showing step heights up to 0.8 mm. The increase in crack velocity successfully decreases the roughness complexity of newly generated surface and drives the fracturing mode from intergranular to transgranular and mode I to mode II. The mist and hackle marks are observed due to crack branching as the crack velocity approaches to the level of Rayleigh wave velocity (Ravi-Chandar and Knauss 1984). Actually, the rate dependency of surface roughness codetermined by two competitive mechanisms including (i) high crack velocity leading to the departure of the crack from its original tip, which causes an increase in fractal dimension in the forms of mists, hackles and microsteps and (ii) the transform to transgranular fracturing resulting in smoother surfaces definitely decreases the fractal property.

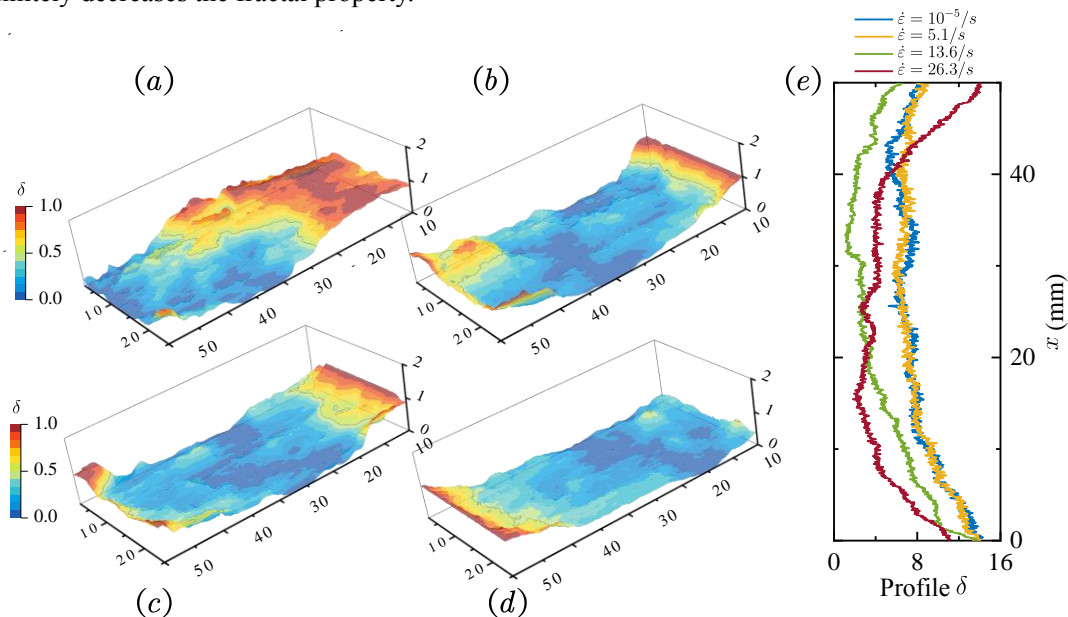


Fig. 4.7 The normalized profiles of fracture surface subject to different strain rates, (a) $\dot{\epsilon}=10^{-5}/s$, (b) $\dot{\epsilon}=5.1/s$, (c) $\dot{\epsilon}=13.6/s$ and (d) $\dot{\epsilon}=26.3/s$, and (e) the experimental fracture profiles on the centerline under different strain rates.

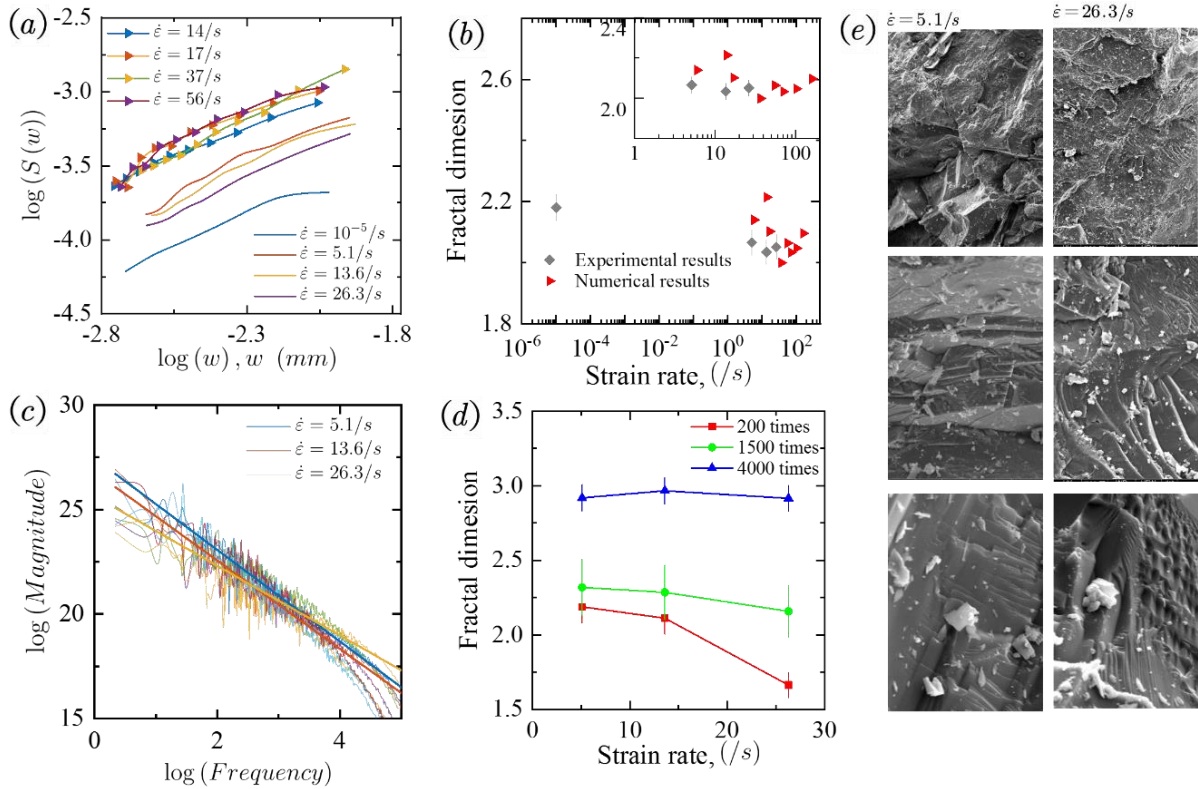


Fig. 4.8 (a) Results of power spectral density with regarding to window size in log-log plot. (b) The experimental and numerical fractal dimension values change with strain rates. (c) Results of power spectral density for SEM images and (d) fractal dimension values as a function of strain rates at different magnification times, (e) the micro fracture characteristic under different strain rates.

5. Uniaxial dynamic compression on rocks: characteristic size, fragment distribution and pulverization law

5.1 Dynamic class I and class II failure types

The dynamic stress-strain curves are categorized into class I and class II by the features of residual strain, fracture pattern and strain rate. Class I is characterized by slightly split or fractured samples loaded at low strain rates. The unloading stage in post-peak induced by the strain recovery indicates the stored energy is not high enough to fracture the sample in such cases. The residual strain, valued about 0.47%, was much lower in comparing to the rupture strain 0.6% (Fig. 5.1). The class I encountered in dynamic loading is a result of insufficient energy input rather than the intrinsic slip weakening of rocks. The recovery of elasticity results from the unloading process and the partial fragmentation is caused by the tensile wave reflected from the free surface of samples.

Samples loaded at critical strain rates below 80/s were found split or fractured and the failure strength is below 175 MPa. The input energy is enough to cause unrecoverable damage to the samples and this damage results in macroscopically fractured debris. Considering the unrecoverable dissipated energy, the recovery stage was not observed on the stress-strain curves and the residual strain was larger than the rupture strain. Exceeding the critical strain rate range, the samples are fractured to fine fragments with an average size below 2.5 mm. In this type (class II), the samples are pulverized by excess energy and the transmitted stress successively decreases after the dynamic fracturing process.

5.2 Strain rate effect and characteristic strain rate

A clear transition zone that separates the rate dependency as class I failure and class II failure is visible (Fig. 5.2 a). The strain rate threshold representing the dynamic pulverization is 80/s. The residual strain is linearly dependent on the increase of fracture strain (Fig. 5.2 b). The final state of the samples transits from slightly splitting to pulverized in association with the relationship between the residual strain and fracture strain.

The failure process of samples can be described as the input energy dissipation (Fig. 5.2 c and Table 5.1).

Experimental results indicate that the dissipated energy density is a linear function of the input energy density and the higher input energy results in higher strain rate. [Fondriest et al \(2017\)](#) infer that the critical dissipated energy density is $\sim 1.8 \text{ J/cm}^3$ and a larger dissipated energy density results in pervasively pulverized damage on samples. This threshold for crystalline rocks such as quartz-monzonite is $\sim 1.5 \text{ J/cm}^3$ ([Aben et al. 2016](#)) and for calcitic marble is $\sim 1.1 \text{ J/cm}^3$ ([Doan and Billi, 2011](#)). The dissipated energy density threshold of granite shown in [Fig. 5.2 c](#) is about 2.0 J/cm^3 .

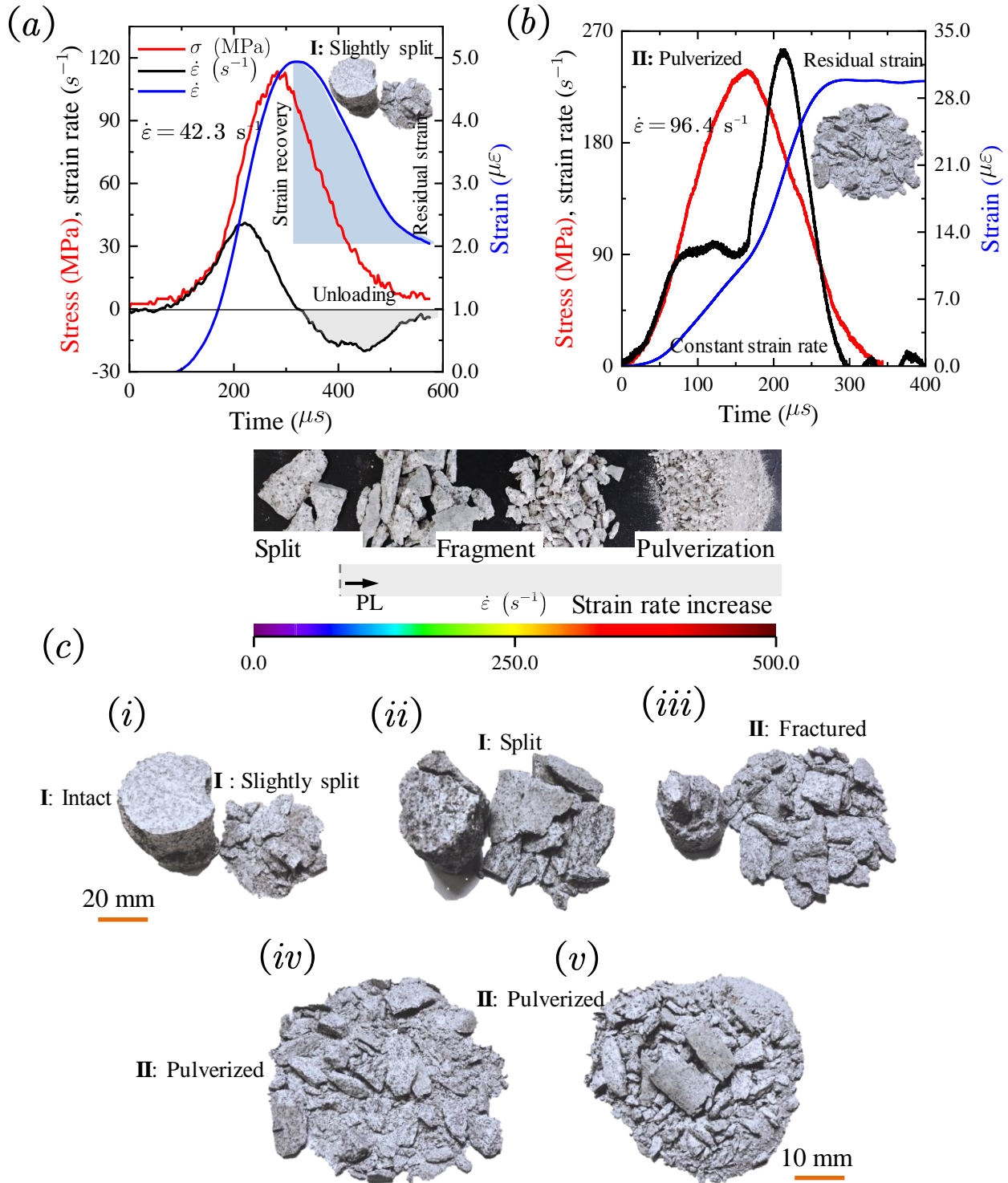


Fig. 5.1 Stress, strain rate and strain curves as functions of time for class I and class II failure. (a). Class I, (b). Class II. (c) Images of the final states showing fragment degree of the granites under different strain rates.

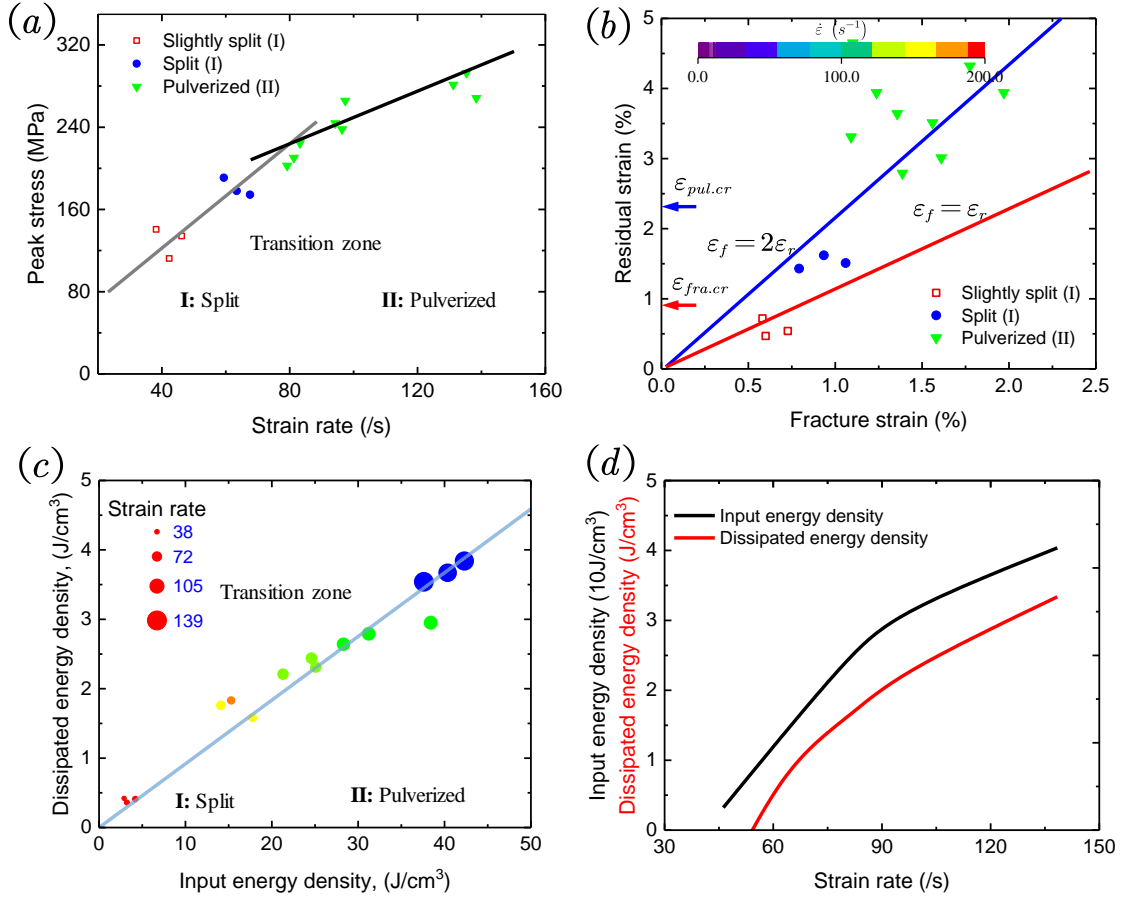


Fig. 5.2 (a) Dynamic peak stress versus strain rate of two types mechanical stress-strain responses. (b) Residual strain versus fracture strain at different dynamic loading conditions. (c) Dissipated energy density as a function of input energy density. (d) Energy densities versus strain rate.

5.3 Fragment distribution and physical-based dynamic fragmentation model

Statistical approaches associated with natural defect initiation, nucleation and coalescence were used to characterize the debris features of brittle materials. Fragmentation distribution is described by a probability function that represents the statistical distribution of the debris number frequency and the cumulative distribution function (CDF) is

$$G(x) = \int_0^x g(x) dx \quad (5.1)$$

With regard to Weibull distribution, the hazard function is considered as $h(x) = \lambda k x^{k-1}$ and the CDF is established as

$$G(x; \lambda, k) = 1 - \exp\left(-\left(\frac{x}{\lambda}\right)^k\right) \quad (5.2)$$

where λ and k are the scale parameter and the shape parameter of the distribution. The distribution of the length scale spans from 0.1 to 10 mm with an increasing probability (Fig. 5.3 and Table 5.2). The peak value of the minor axis increases significantly when the strain rate increases from 42.3 to 131.2 /s (Fig. 5.3 c and d). This rate dependency results in distinct characteristics of the size distribution including: (i) increasing the percentage of the scale size and reducing the width of the distribution; (ii) reducing the scale size from 10.4 mm to 1.01 mm; and (iii) gathering the debris size distribution and resulting in lower variance.

The strain rate range in this study is from 40 to 150/s and the average fragment size ranges from 1.0 to 13 mm (Fig. 5.5). The new presented model agrees well with the results of shattered granite samples. The results of the theory predictions indicate that:

- (i) The dynamic fragmentation has two regimes separated by the characteristic strain rate. The fragment size in the lower strain rate regime is constant, which is determined by the strain energy.
- (ii) The critical strain rate predicted by the present model is about 10/s. The fragmentation under critical strain rate is

strain energy controlled and the strain rate influence on the breakage of solids is limited. The regime over the critical strain rate is kinetic energy controlled and the rate dependency of fragment size is stronger than other models predicted.

(ii) In previous models, the fragment size is controlled by expanding kinetic energy at high enough strain rates. This model includes the compression kinetic energy and the characteristic size is codetermined by kinetic energy and strain energy.

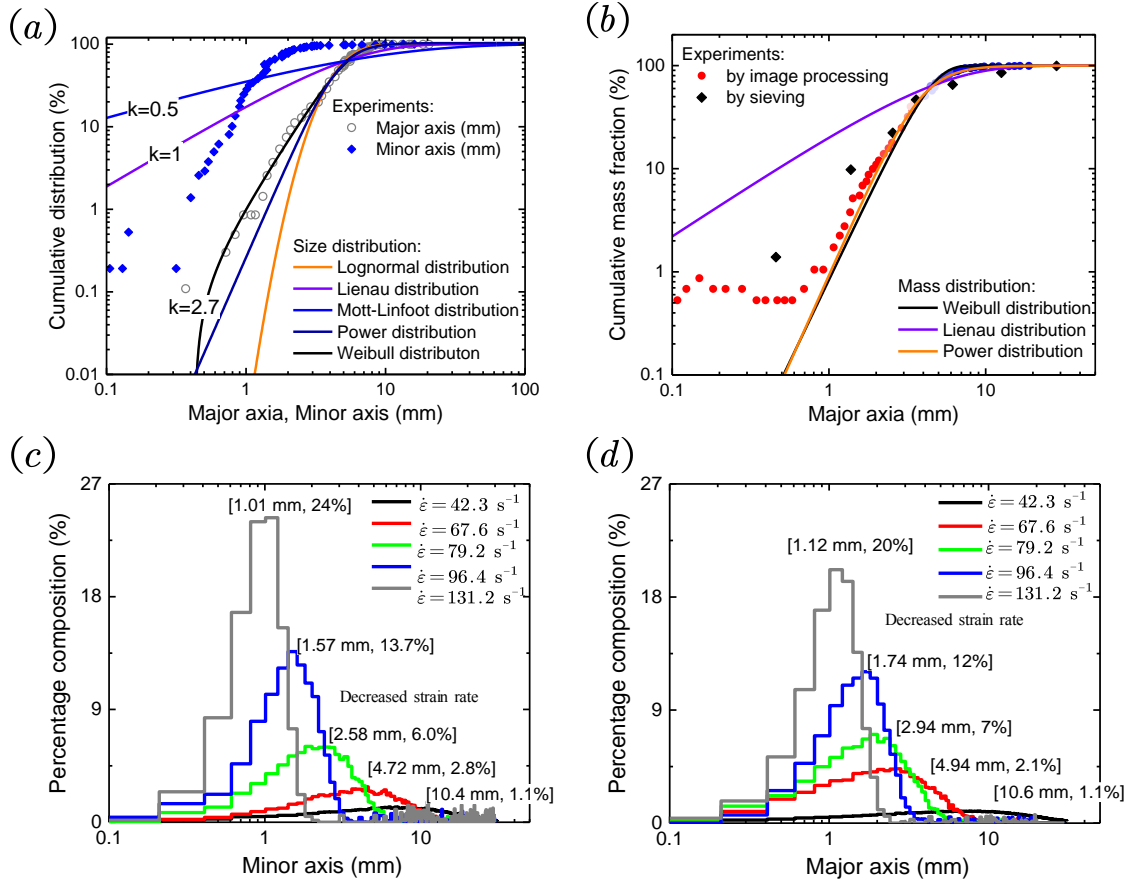


Fig. 5.3 Example images of cumulative fragment size distribution of sample DG11 and different fitting distributions.

Table 5.1 Summary of the experimental results at different strain rates

Sample No.	e_i (J)	e_d (J/cm ³)	$\dot{\epsilon}$ (/s)	σ_{dyn} (MPa)	ϵ_p (%)	ϵ_r (%)	DIF	Failure mode
UCSG2	—	—	1e-5	129.0	0.34	—	—	Split
DG1	316	0.36	42.3	111.4	0.6	0.47	0.87	Slightly split
DG5	1384	1.76	67.6	173	1.06	1.51	1.35	Slight fractured
DG9	2461	2.31	79.2	201	1.61	3.01	1.57	Fractured
DG11	3064	2.79	96.4	236.1	1.56	3.51	1.84	Pulverized
DG12	3961	3.67	131.2	279.1	1.97	3.94	2.18	Pulverized

Note: $\sigma_{sta} = 129$ MPa, $\epsilon_{str} = 0.34\%$.

Table 5.2 The fragment results of the samples at different strain rates

Sample No.	$\dot{\epsilon}$ (/s)	s (mm)	Size λ	Size k	Mass λ	Mass k	Characteristic mass (g)	Area (mm ²)
DG1	42.3	13	14.5	2.17	16.2	1.49	14.6	428.6
DG5	67.6	3.2	3.6	1.81	5	1.2	4.8	28.3
DG9	79.2	2.22	2.51	1.64	3.6	1.4	3.3	16.7
DG11	96.4	1.6	1.79	1.25	2.8	1.2	2.6	10.3
DG12	131.2	1.03	1.16	1.01	3.1	0.5	6.7	4.1

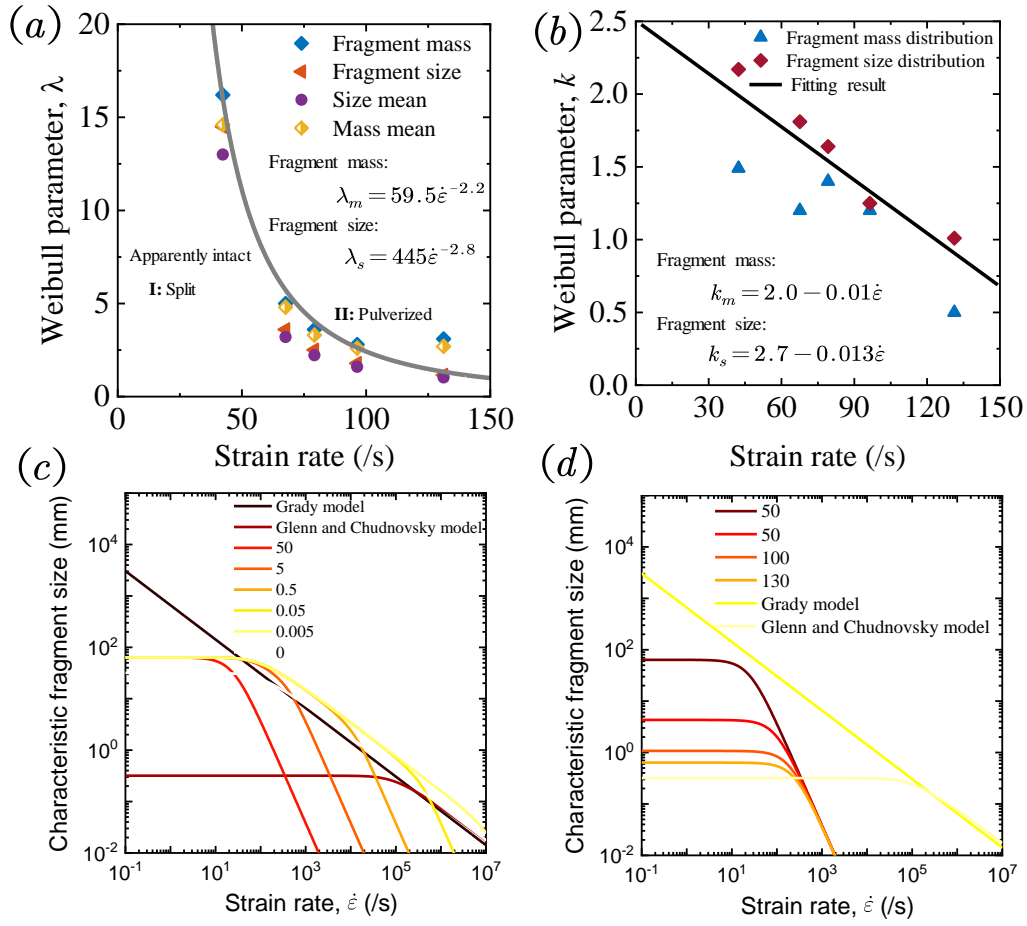


Fig. 5.4 The dependence of: (a) scale parameter and (b) shape parameter on the strain rate. The influence of the (c) fracture strength and (d) axial fragment length on the fragment model.

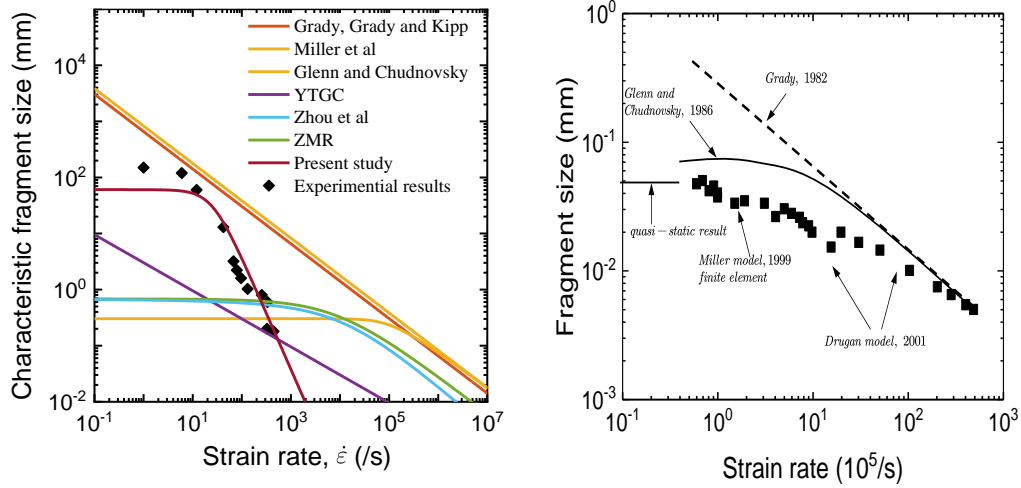


Fig. 5.5 Physical-based fragmentation theories and experimental results.

6. Unified dynamic strength model of fractured rock: insights from the theoretically dynamic fracturing model

6.1 Dynamic sliding crack model

The crack kinking angle violates the laboratorial results when the wing crack is small in shear sliding model (Nemat-Nasser and Horii 1982). To overcome this defect, we propose a novel model assuming that the normalized wing crack angle is a function of crack length $\theta(\ell) = \theta e^{-(\ell/\ell_0)}$ and the modified stress intensity factor is

$$\mathcal{K}_I = \frac{2c\tau_e \sin \theta}{\sqrt{\pi(l+l^*)}} \underbrace{\cos \frac{\theta(\ell)}{2}}_{\text{transition}} - \sigma_n \sqrt{\pi l} \quad (6.1)$$

where $2c$ is the crack length and l is the length of wing crack. τ_e and σ_n' are the effective shear stress and normal stress on the crack surface. The intensity factor enhancement coefficient is considered to account for the effect of crack velocity

$$k(i) = \left(1 - \frac{i}{c_R}\right)^\alpha \quad (6.2)$$

6.2 Description of strain

Consider an isothermal deformation process of an elastic solid weakened by a number of initially distributed microcracks. The flaw is compressed by external stress σ_1 and σ_3 and the angle of wing crack is θ . The effective stress on the crack face are

$$\begin{bmatrix} \sigma_n \\ \tau \end{bmatrix} = \begin{bmatrix} \sin^2 \gamma & \cos^2 \gamma \\ \sin \gamma \cos \gamma & -\sin \gamma \cos \gamma \end{bmatrix} \begin{bmatrix} \sigma_1 \\ \sigma_3 \end{bmatrix} \quad (6.3)$$

Because the tensile strength of rock is much lower than the compressive strength, the maximum hoop stress criterion is used to determine the crack initiation direction $\partial \sigma_{\theta\theta} / \partial \theta = 0, \partial^2 \sigma_{\theta\theta} / \partial \theta^2 < 0$.

The fracturing propagation of microcracks are divided into four stages:

Stage one: Elastic deformation. The crack is closed prior to crack initiation when the principal stress $\sigma_1 < \sigma_{slip}$. The strain is

$$\varepsilon = \varepsilon_{ij}^e \quad (6.4)$$

Stage two: Onset of crack initiation. Shear sliding occurs when the effective shear stress exceeds σ_{slip} , potential microcracks are activated when $\sigma_{slef,II} > \sigma_1 > \sigma_{slip}$, the range of inclined cracks is identified as $\Omega_{slip} = \tau_e > 0$. The strain is

$$\begin{aligned} \varepsilon_{kl}^{(c1)} &= f^{(\alpha)} 2b \left(\frac{\partial \tau_f}{\partial \sigma_{ij}} + \frac{\partial \tau_e}{\partial \sigma_{ij}} \right) \\ \varepsilon &= \varepsilon_{ij}^e + \int_{\gamma_{slip}^1}^{\gamma_{slip}^2} p(\gamma) \varepsilon_{ij}^{(c1)} d\gamma \end{aligned} \quad (6.5)$$

Stage three: Self-similarly sliding. The crack develops self-similarly along the crack surface in the range of $[\sigma_{slip}, \sigma_{kink})$. The propagation strain is divided into two parts: primary crack slip and secondary crack slip. The strain is

$$\begin{aligned} \varepsilon_{ij}^{(c2)} &= f^{(\alpha)} 2b \frac{\partial \tau}{\partial \sigma_{ij}} + f^{(\alpha)} 2\ell \frac{\partial \tau}{\partial \sigma_{ij}} \\ \varepsilon &= \varepsilon_{ij}^e + \varepsilon_{ij}^{(c1)} + \int_{\gamma_{slef,II}^1}^{\gamma_{slef,II}^2} p(\gamma) \varepsilon_{ij}^{(c2)} d\gamma \end{aligned} \quad (6.6)$$

Stage four: Wing crack kinking. The main crack deflects when the stress exceeds the kinking stress σ_{kink} (in Fig. 6.2). The equivalent stress intensity factor is

$$\mathcal{K}_I = \frac{-\tau_e 2c \sin \gamma}{\sqrt{\frac{w}{2} \sin\left(\frac{2\pi(l+l^*)}{w}\right)}} + \sigma_3 \sqrt{w \tan\left(\frac{\pi l}{w}\right)} \quad (6.7)$$

The strain in this stage is

$$\varepsilon = \varepsilon_{ij}^e + \varepsilon_{ij}^{(c1)} + \varepsilon_{ij}^{(c2)} + \int_{\gamma_{kink}^1}^{\gamma_{kink}^2} p(\gamma) \varepsilon_{ij}^{(c3)} d\gamma \quad (6.8)$$

6.3 Crack interaction

Considering the crack interaction in the double offset crack model, the n th crack stress intensity factor is approximated as

$$\mathcal{K}_I \approx \mathcal{K}_I^0 \left(1 + \sum_{k=1}^{\infty} \frac{1}{2} \left(\frac{c+l}{kw} \right)^2 (2 \cos 2\varphi_k - \cos 4\varphi_k) \right) \quad (6.9)$$

For the superposition in the finite field $\sum_{k=1}^{\infty} ((c+l)/kw)^2$, the above equation is approximated to $\sum_{k=1}^{\infty} (l/kw)^2$ when $l \gg c$. The approximate solution of the multi-crack body considering the interaction is

$$\frac{\mathcal{K}_I^{int}}{\mathcal{K}_I^0} = \left(1 + \alpha \left(\frac{l}{w}\right)^\beta\right) f(\varphi) \quad (6.10)$$

where $f(\varphi)$ is the influence coefficient of the offset angle between two neighboring cracks.

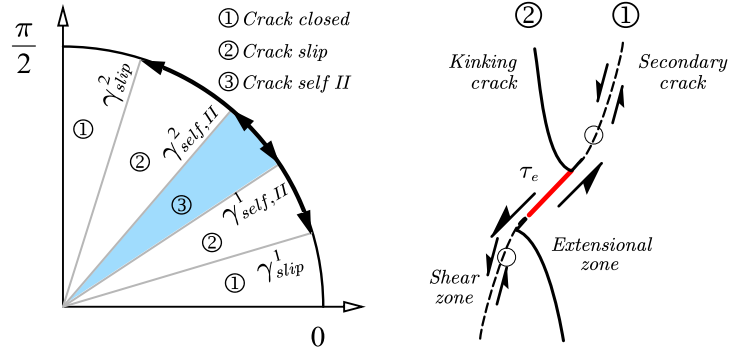


Fig. 6.1(a) Domains of the crack self-sliding, (b) conditions for self-similar and kinking of main crack tips.

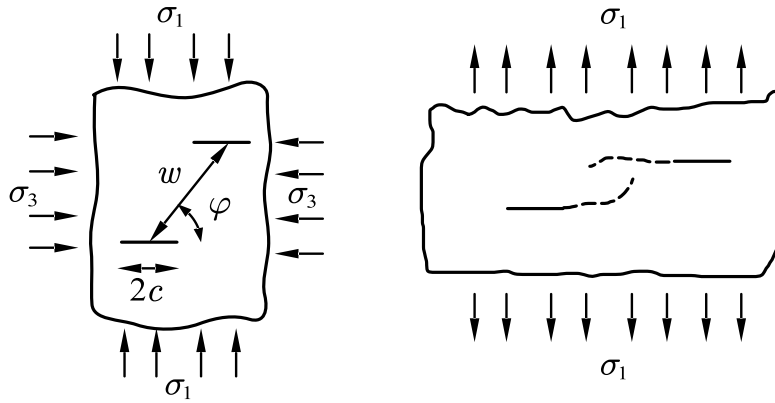


Fig. 6.2 (a) Two interacting cracks, (b) interaction between two cracks propagating towards each other.

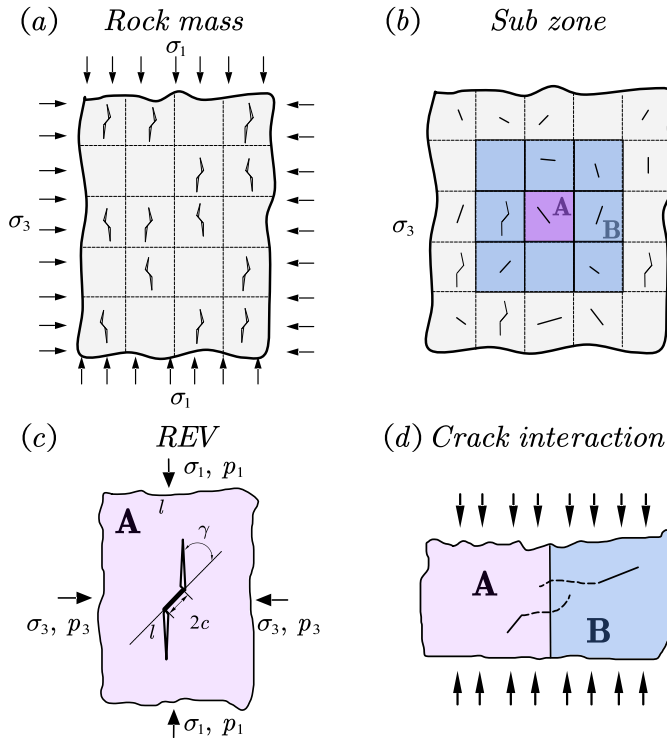


Fig. 6.3 Multi-crack interaction model for stochastic fractured rock mass.

6.4 The dynamic sliding crack model for fractured rocks

The randomness of fractured rocks includes: (i) the randomness of crack spatial location; (ii) the randomness of crack inclination; (iii) the randomness of crack length. It is assumed that the crack angle follows a uniform distribution

$$p(\gamma) = H\left(\frac{\pi}{2} - |\gamma|\right) \frac{1}{\pi} \quad \forall \gamma \in \left[-\frac{\pi}{2}, \frac{\pi}{2}\right] \quad (6.11)$$

The Weibull distribution is used to represent the crack length, and the density function of the length is

$$g(c) = H(c) \frac{m}{n} \left(\frac{c}{n}\right)^{m-1} \exp\left(-\left(\frac{c}{n}\right)^m\right) \quad (6.12)$$

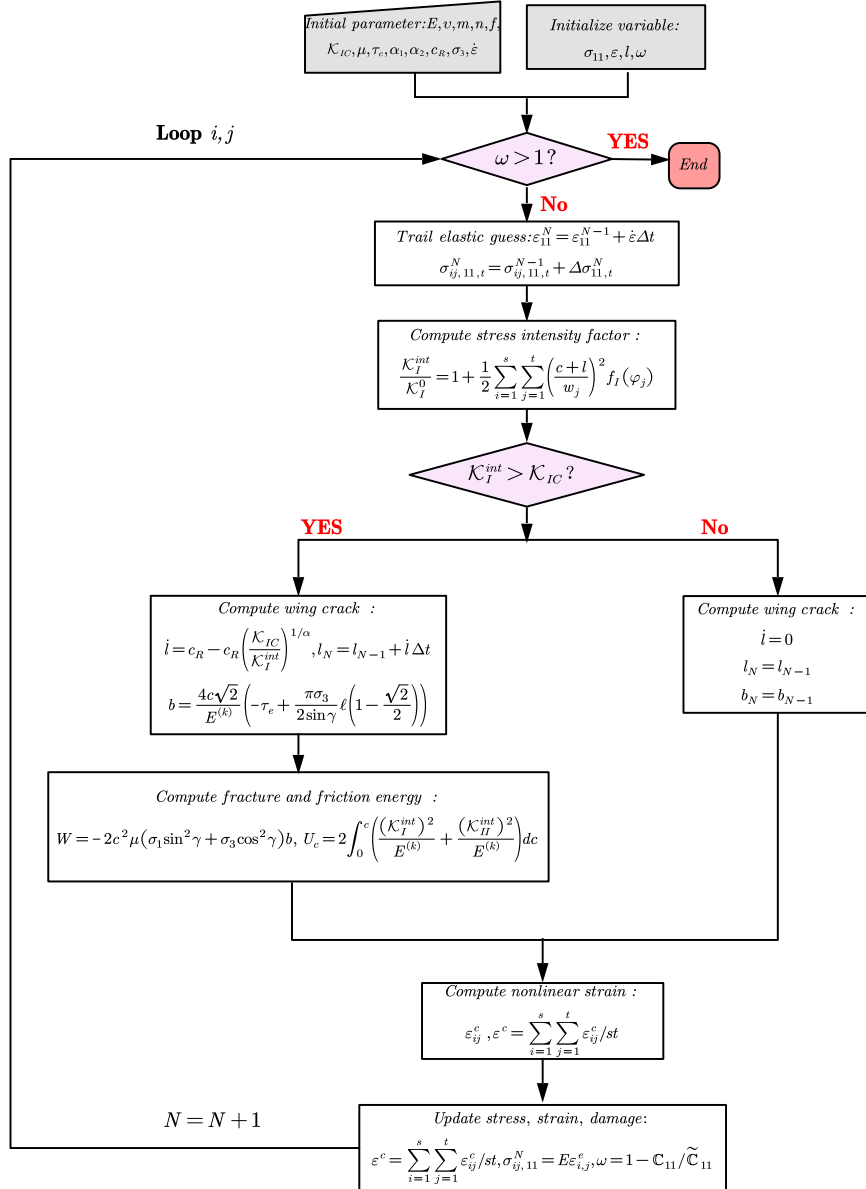


Fig. 6.4 Flow chart for stress-strain constitutive calculation of multi-fractured rock mass.

The crack angle and crack radius in different REVs are simulated by Monte Carlo method. Assuming that each crack is affected by surrounding REVs, the relationship between the cracks is expressed as

$$\frac{K_I^{int}}{K_I^0} = 1 + \frac{1}{2} \sum_{i=1}^s \sum_{j=1}^t \left(\frac{c+l}{w_j}\right)^2 f_I(\varphi_j) \quad (6.13)$$

where i is the REV layer number surrounding the main crack, j is the REV number of the i th layer. Taking the

first layer as an example, there are 8 REVs around the crack A, and the corresponding t is 8, and the variation range is 1, 2, 3.... The number of REVs in the second layer is 16, the number of REVs in the third layer is 24, and so on. However, when the number of layers becomes larger, the REV spacing in Eq. (6.13) becomes larger and the interaction between cracks is attenuated. To simplify the computation, only the first three layers are selected in this study.

The nonlinear strain of a single crack is obtained due to the Catigiano energy balance principle. The multicrack model is calculated by superimposing single cracks. The basic governing equations are shown in Fig. 6.4.

6.5 Unified dynamic strength model

In this thesis, the theoretical mechanical properties under four confining pressure $\sigma_3=5.0, 10.0, 20.0$ and 30.0 MPa are validated (Fig. 6.5). As the confining pressure increases, the failure strength shows obvious enhancement characteristics. From the dilatancy behaviour of the material, the increase in confining pressure reduces the lateral deformation and volume expansion of the rock, and even shear shrinkage occurs at a higher confining pressure value. It can be found that the crack initiation stress does not change significantly with the increase of confining pressure, but the crack damage stress increases significantly with the increase of confining pressure.

The peak stress increases significantly with the increase in strain rate, and the strength increases rapidly from 145 MPa in quasi-static ($10^{-3}/s$) to 445 MPa in the strain rate of $1000/s$ (in Fig. 6.6). The stress strengthening is mainly caused by the main crack sliding and wing crack propagation, while the strain softening in post-peak is a result of crack interaction. The nonlinear deformation before the peak significantly increases with the increase of the strain rate. The failure of the rock at low strain rate is mainly dominated by brittle fracturing, and the damage value corresponding to the peak stress is 0.1. The strain rate further strengthens the damage threshold by changing the crushing properties of the material, leading to further improvement of the thresholds for irreversible damage.

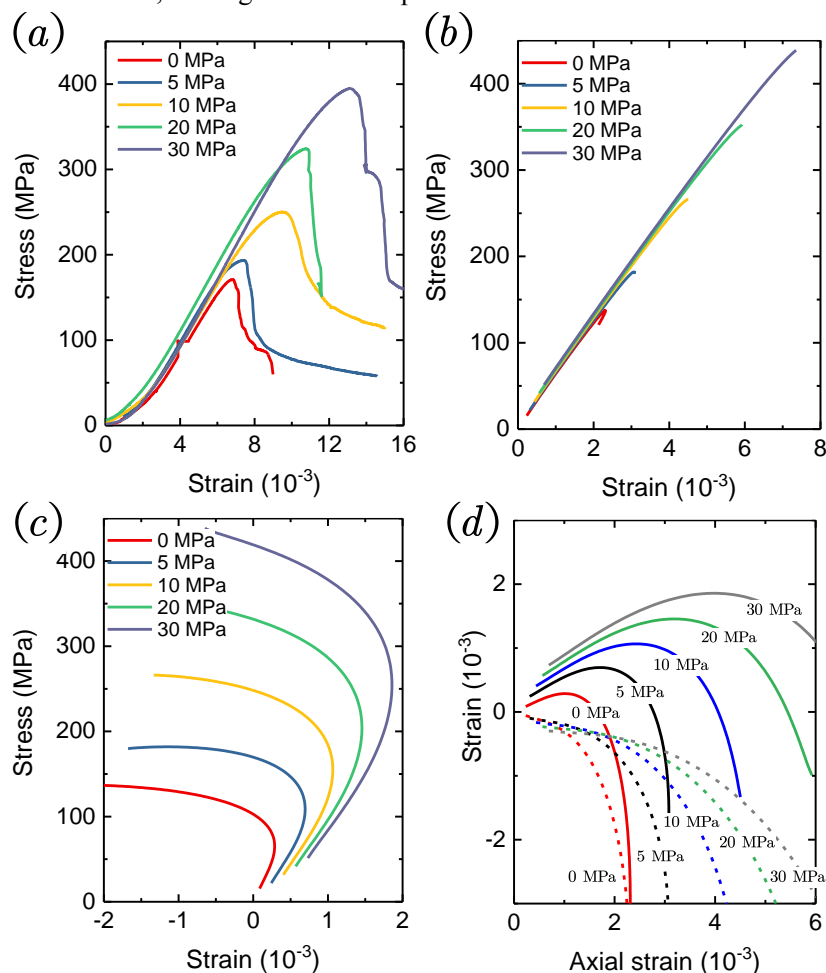


Fig. 6.5 Comparisons between theoretical model calculation results and experimental results under different confining pressures: (a) experimental results, (b) theoretical results, (c) theoretical transverse strain-stress curve, (d) crack strain and volume strain curve.

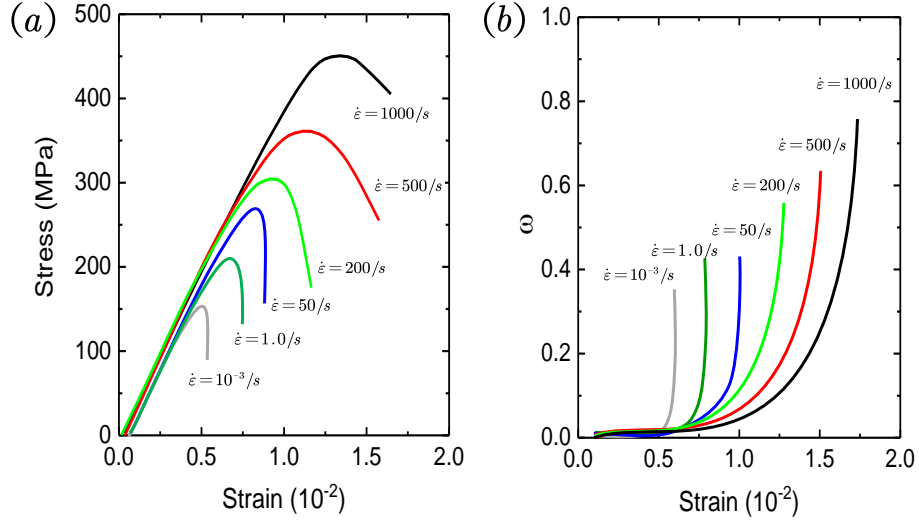


Fig. 6.6 (a) Stress-strain curves at different strain rates, (b) relationship between damage variables and stresses at different strain rates.

The fracture strength is depended on eight variables according to Buckingham π -theorem

$$\sigma_f = f(E, m_i, \mathcal{K}_{IC}, \rho, c, f, \dot{\epsilon}, c_p) \quad (6.14)$$

The physical equations between the variables should satisfy: (i) when the strain rate is infinitely small $\sim 10^{-5}/s$, the dynamic increase factor approaches to 1.0; (ii) the characteristic strain rate of rock material is in the range of $1 \sim 500/s$, and the strain rate increase factor varies between 1/3 and 1.0.

The relationship between the crack geometric characteristics and the fracture strength is

$$\frac{\pi_2}{\pi_6} = 1 + (\pi_4)^\beta \quad (6.15)$$

where the characteristic strain rate is $\dot{\epsilon}_c = \pi_4/\dot{\epsilon}$, which is composed of three parts: the ultimate strain at failure $\mathcal{K}_{IC}/c^{1/2}E$, the approximate time within the crack propagation interval c_p/s , and the initial damage effect c/s .

Therefore, the unified dynamic strength law is normalized as

$$\frac{\sigma_y}{\sigma_c} = 1 + \left(\frac{\dot{\epsilon}}{\dot{\epsilon}_0}\right)^\alpha \quad (6.16)$$

where σ_y, σ_c are the dynamic and static strength of rock (MPa), $\dot{\epsilon}_0$ is the characteristic strain rate of rocks (/s), α is the strain rate increase factor. The characteristic strain rate is

$$\dot{\epsilon}_0 = \chi \frac{K_{IC}}{Ec^{1/2}} \frac{c_R}{s} \frac{c}{s} \quad (6.17)$$

which is determined by the crack spacing and crack length. The strain rate increase factor is

$$\alpha = \frac{1}{1+n} \quad (6.18)$$

where n is the crack propagation factor is denoted as $v = \beta K_I^n$.

6.6 Scaling of the rate-dependent strength

DIF of different rocks under compression is plotted as a function of strain rate, as shown in Fig. 6.7. The results show that the change of DIF can be divided into slight rate dependence and strong rate dependence. In this study, we use the unified dynamic strength model to characterize the strain rate dependency. The regressed result presented as $DIF = 1 + (\dot{\epsilon}/154)^{0.54}$ has the best regression value $R^2=0.96$ and the rate-insensitive response at intermediate strain rate also can be well presented at the same time.

A summary of the available experimental data for different rocks in dynamic tension tests is presented in Fig. 6.8. In the plot, the direct tension results show lower rate sensitivity in comparing with the results carried out by other indirect methods. The spalling tests have the largest values of the dynamic increase factor due to the coupling of the inertia stress within the fractured strength.

With a focus on the characteristic strain rate change for different rocks, a summary of the DIF at different strain rates is carried out. The regressed results of characteristic strain rate and strain rate increase factor for some geological

materials are presented in Table 6.1. The values listed in Table 6.1 provide useful tools for estimating the strain-rate effect of different rocks.

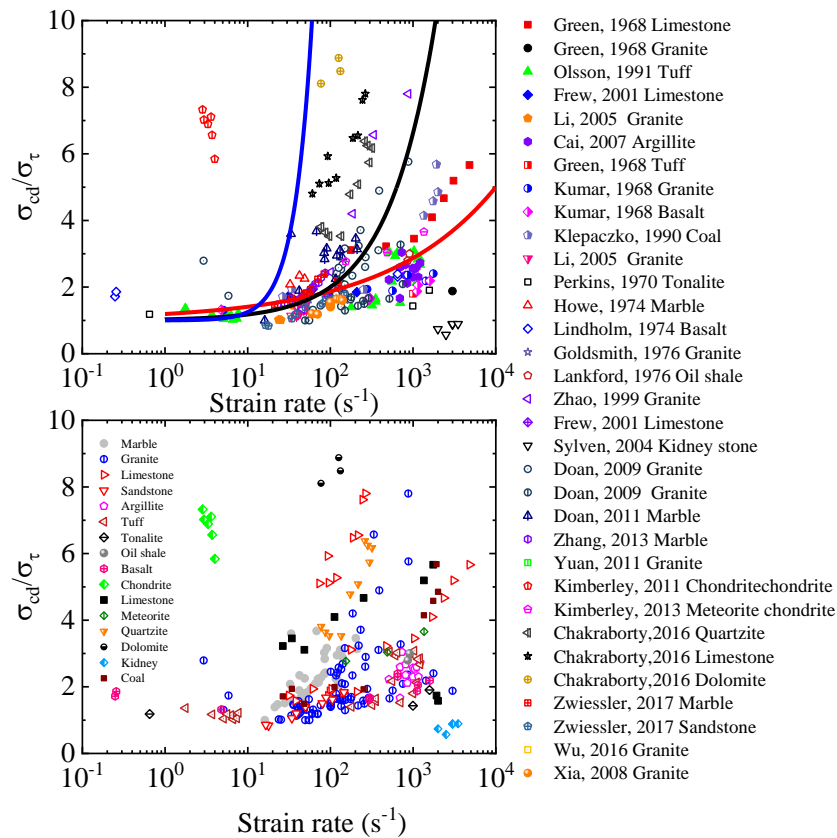


Fig. 6.7 A summary of the dynamic increase factor for rocks as a function of strain rates in compression.

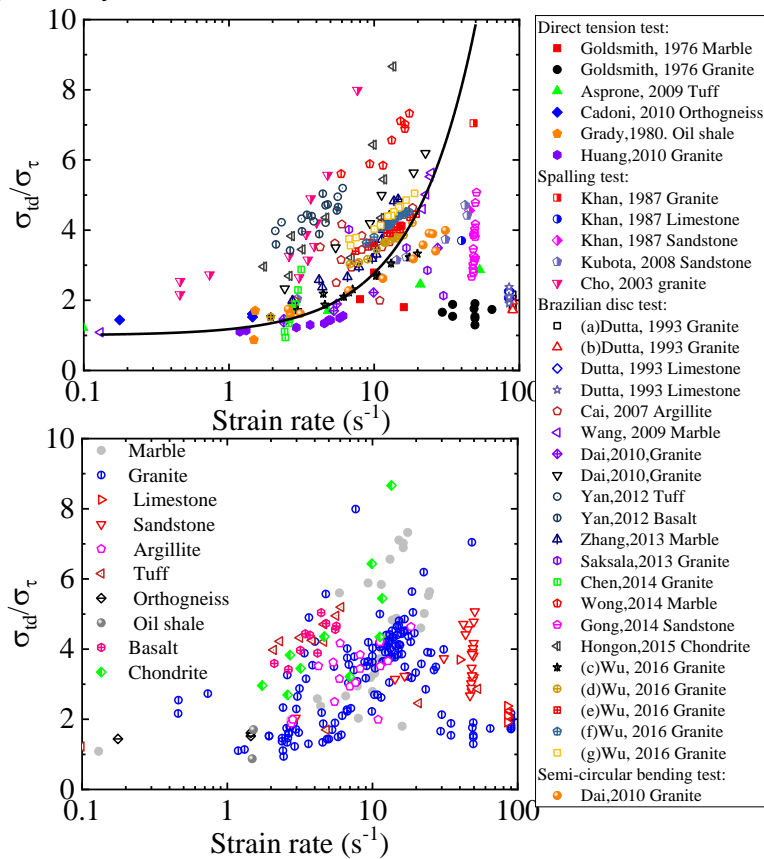


Fig. 6.8 A summary of the dynamic increase factor for rocks as a function of strain rates in tension.

Rock type	Characteristic strain rate (/s)		Strain rate increase factor	
	Compression	tension	Compression	tension
Marble	50 ± 3	1.2 ± 0. 2	0.79	0.55
Limestone	75 ± 12		0.75	
Coal	140 ± 15		0.6	
Granite	160 ± 21	2.1 ± 0. 3	0.47	0.53
Tuff	160 ± 16	0.15 ± 0. 1	0.31	0.35
Chondrite	170 ± 17	0. 87 ± 0. 04	0.58	0.63
Meteorite	190 ± 23		0.56	
Sandstone	200 ± 32	2.0 ± 0. 3	0.5	0.36
Mudstone		1.2 ± 0. 1		0.47
Basalt		0.2 ± 0. 3		0.4

7. Transgranular fracturing of rocks and development of a grain-scale continuum-discontinuum approach

7.1 Voronoi tessellation of the grain-based modelling

The Voronoi tessellation is used for the multiscale grain-based continuum-discontinuum method (GbCDM) to generate the heterogeneous model that incorporates the grain morphology of rocks in this study. Considering a set of seed points G_i in 2D domain D ($D \in \mathbb{R}^2$), every seed is associated with a Voronoi cell as

$$C_i = [P(\mathbf{x}) \in D \mid \text{dist}(P, G_i) < d(P, D_j) \quad \forall j \neq i] \quad (7.1)$$

where $\text{dist}()$ is the Euclidean distance and the seed positions are randomly located in domain D according to a random distribution. The Voronoi polygon is convex, and the intersection between two polygons is treated as a grain boundary. The Voronoi morphologies were determined by cell sphericity and diameter (Fig. 7.1 and Fig. 7.2).

7.2 Mathematical model of hybrid continuum-discontinuum method

7.2.1 Weak formulation of updated Lagrange

Consider an arbitrary body $\Omega \subset \mathbb{R}^D$ ($D \in \{1, 2, 3\}$), \mathbf{x} is the current position vector of the point and $\mathbf{u}(\mathbf{x}, t) \subset \mathbb{R}^D$ is the displacement at time $t \in [0, t_{all}]$. The conservation of momentum is

$$\rho \ddot{\mathbf{u}}(\mathbf{x}) - \nabla \cdot \boldsymbol{\sigma} - \mathbf{b} = 0 \quad \text{in } \forall \mathbf{x} \in \Omega \quad (7.2)$$

Therefore, the discretised virtual work expression considering the kinetic is

$$\int_{\Omega} [\boldsymbol{\sigma}^T \mathcal{B}^g \delta \mathbf{v} - (\mathbf{b} - \rho \ddot{\mathbf{u}}) \cdot \mathcal{N}^g \delta \mathbf{v}] d\Omega - \int_{\partial^* \Omega} \mathbf{t} \cdot \mathcal{N}^g \delta \mathbf{v} d\Omega = 0 \quad \text{in } \forall \delta \mathbf{v} \in \Omega \quad (7.3)$$

Since the above equation is satisfied for all vectors $\delta \mathbf{v}$, equation (7.3) can be reformulated as

$$\mathbf{M}^{\text{FE}} \ddot{\mathbf{u}} + \mathbf{f}^{\text{int}}(\mathbf{u}) - \mathbf{f}^{\text{ext}} = \mathbf{0} \quad (7.4)$$

while the internal force $\mathbf{f}^{\text{int}}(\mathbf{u})$, external force \mathbf{f}^{ext} and inertia mass \mathbf{M}^{FE} are

$$\mathbf{f}^{\text{int}}(\mathbf{u}) = \int_{\Omega} (\mathcal{B}^g)^T \cdot \boldsymbol{\sigma}(\mathbf{u}) d\Omega \quad (7.5)$$

$$\mathbf{f}^{\text{ext}} = \int_{\Omega} (\mathcal{N}^g)^T \rho \mathbf{b} d\Omega + \int_{\partial^* \Omega} (\mathcal{N}^g)^T \mathbf{t} d\Omega = 0 \quad (7.6)$$

$$\mathbf{M}^{\text{FE}} = \int_{\Omega} (\mathcal{N}^g)^T \rho \mathcal{N}^g d\Omega \quad (7.7)$$

\mathcal{B}^g and \mathcal{N}^g are matrices incorporating the interpolation functions and their spatial derivatives in global, respectively.

7.2.2 Penalty stiffness contact force

To identify whether the two blocks target Ω_{β_t} and contractor Ω_{β_c} are contacted, we define two points in block (t) $p(\mathbf{x}^{(t)} \mid \mathbf{x}^{(t)} \in \Omega_{\beta_t})$ and block (c) $p(\mathbf{x}^{(c)} \mid \mathbf{x}^{(c)} \in \Omega_{\beta_c})$. The position vector of the centres of the particles are $\mathbf{x}^{(c)}$ and $\mathbf{x}^{(t)}$, and the original position vectors of the two particles are $\hat{\mathbf{x}}^{(c)}$ and $\hat{\mathbf{x}}^{(t)}$ (in Fig. 7.3). The condition of

overlapping is

$$g = \min \left\{ \begin{array}{l} |\mathbf{x}^{(t)} - \mathbf{x}^{(c)}| \\ \forall \mathbf{x}^{(t)} \in V_t, \forall \mathbf{x}^{(c)} \in \partial\Omega_{\beta_i} \\ \forall \mathbf{x}^{(t)} \in \partial\Omega_{\beta_i}, \forall \mathbf{x}^{(c)} \in V_c \end{array} \right\} < g_{ref} \quad (7.8)$$

where g is the minimum distance between two block and g_{ref} is the allowing contact gap in numerical computation. $\partial\Omega_{\beta_i}$ and $\partial\Omega_{\beta_c}$ are boundaries of block i and block j , and V_t and V_c are vertex list on the boundaries of block i and block j .

The displacement vectors are taken from

$$\begin{aligned} \mathbf{u} &= \mathbf{x}^{(c)} - \mathbf{x}^{(t)} - (\mathbf{x}^{(c)} - \mathbf{x}^{(t)}) \\ \mathbf{u}_n &= (\mathbf{u} \cdot \mathbf{n}) \cdot \mathbf{n} = (|\dot{\mathbf{x}}^{(c)} - \dot{\mathbf{x}}^{(t)}| - |\mathbf{x}^{(c)} - \mathbf{x}^{(t)}|) \cdot \mathbf{n} \quad \mathbf{x}^{(c)} \in \Omega_{\beta_c}, \mathbf{x}^{(t)} \in \Omega_{\beta_i} \\ \mathbf{u}_t &= (\mathbf{u} \cdot \mathbf{t}) \cdot \mathbf{t} = \mathbf{u} - \mathbf{u}_n \end{aligned} \quad (7.9)$$

with the unit vector in normal direction $\mathbf{n} = \frac{\mathbf{x}^{(c)} - \mathbf{x}^{(t)}}{|\mathbf{x}^{(c)} - \mathbf{x}^{(t)}|}$ and the unit vector in the tangential direction is $\mathbf{t} = \mathbf{s} \wedge \mathbf{n}$,

the superscripts (ab) means the contact between block a and block b . Therefore, the relative velocity vector between blocks is

$$\dot{\mathbf{u}} = \dot{u}_n \mathbf{n} + \dot{u}_t \mathbf{t} \quad (7.10)$$

The forces \mathbf{f} are

$$\mathbf{f} = \mathbf{f}_n + \mathbf{f}_t \quad (7.11)$$

\mathbf{f}_n and \mathbf{f}_t are normal and tangential forces of the contact between block (c) and (t)

$$\begin{aligned} \mathbf{f}_n &= c_n (\mathbf{u} \cdot \mathbf{n}) \mathbf{n} + \gamma_n (\dot{\mathbf{u}} \cdot \mathbf{n}) \mathbf{n} \\ \mathbf{f}_t &= \min(|c_t (\mathbf{u} \cdot \mathbf{t}) \cdot \mathbf{t} + \gamma_t (\dot{\mathbf{u}} \cdot \mathbf{t}) \cdot \mathbf{t}|, |\mu_c \mathbf{f}_n|) \mathbf{t} \end{aligned} \quad (7.12)$$

A is the area of contact, c_n and c_t are the penalties of the contact in normal and tangential directions, respectively. γ_n and γ_s are the corresponding damping coefficients and μ_c is the friction factor.

7.2.3 Contact algorithm

The contact detection algorithm is developed for blocks with evident size using the square bounding box method in cooperation with the NBS algorithm (in Fig. 7.4), which aims to divide the NBS model into several groups (in Table 7.1), the flow chart of the enhanced NBS algorithm is

$$\mathbf{x}^k = 1 + \text{int} \left(\frac{\mathbf{x}_i - \mathbf{x}_{\min}}{d(0)} + \frac{1}{2} \right) \quad (7.13)$$

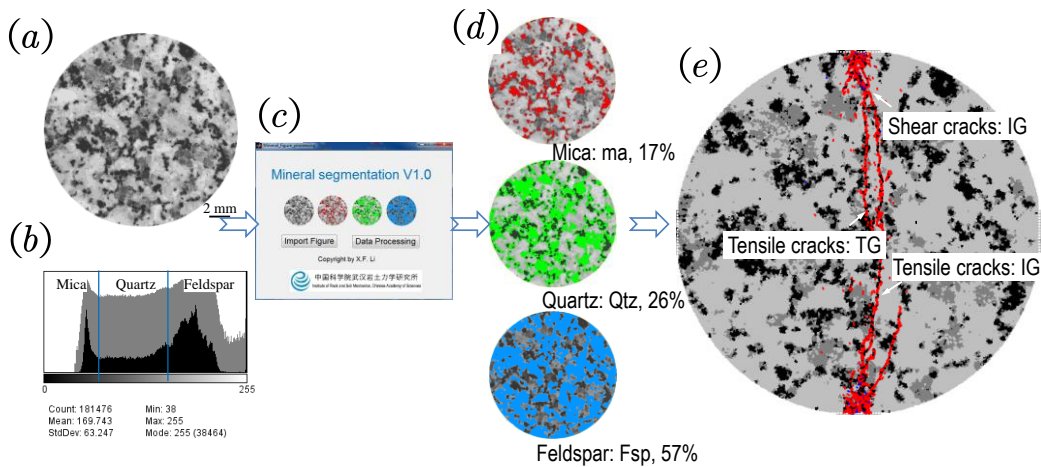


Fig. 7.1 The image-based processing of realistic grain morphology in 2D rGbCDM.

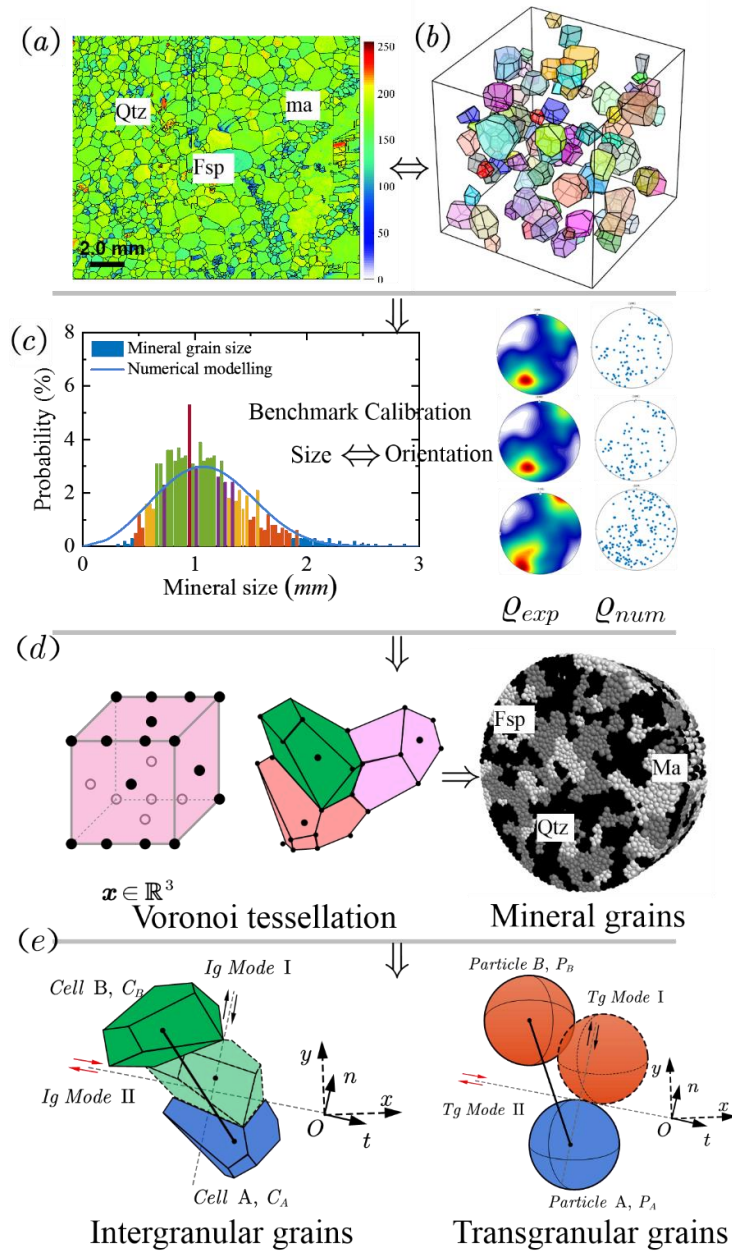


Fig. 7.2 The flow chart of generating Voronoi tessellations according to experimental results in 3D mGbCDM.

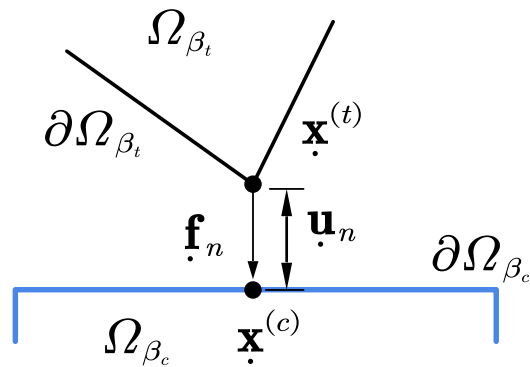


Fig. 7.3 Illustrations of contact force between two blocks in mGbCDM.

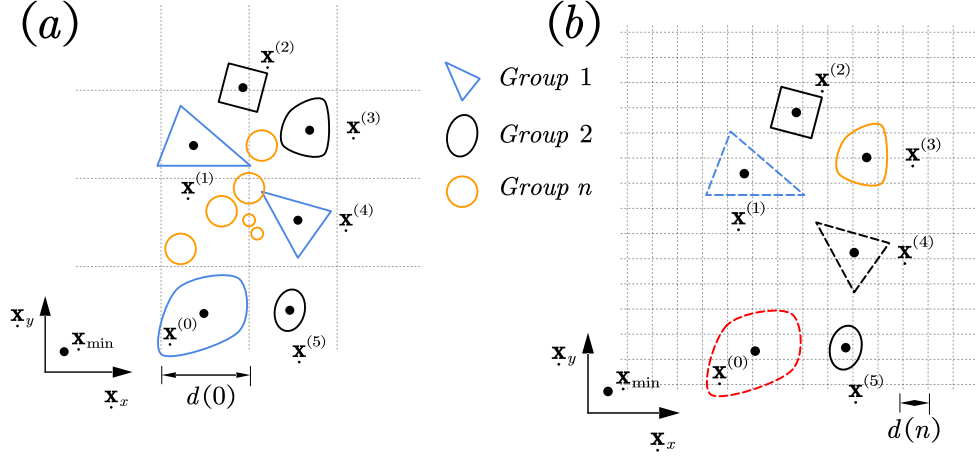


Fig. 7.4 The schematic algorithm of NBS contact detection in mGbCDM.

Table 7.1 The enhanced NBS contact detection method used in mGbCDM

<p>Step 1: Loop the blocks and find the maximum size buffer box for the initial group box $d(0) = d_{\max}$;</p> <p>Step 2: Divide the blocks into n groups with size of buffer box for the nth group box as $d(n) = d_{\max} \cdot \alpha^{n-1}, \alpha \in (0, 1]$;</p> <p>Step 3: All the blocks are mapped in to the grid space with edge length of $d(0)$ as depicted in Fig. 7.4, the central point of the block \mathbf{x}^k is computed in Eq (7.14);</p> <p>Step 4: Loop all the blocks and detect contacts for the first group, the contact couple groups is identified when $\mathbf{x}^{(t)} - \mathbf{x}^{(c)} < \max(d^{(t)} + d^{(c)})$, the contact state can be recognized as neighboring contacts or center contacts;</p> <p>Step 5: Repeat step 3 and step 4 for all groups of the remaining blocks and identify the states of the contacts;</p>
--

7.3 Constitutive laws of inter- and trans- granular cracks

It is noted that the tensile strength in normal direction of intergranular contact is $\sigma_{IG,n}^{cri}$ and the bonded contact breaks when the normal stress exceeds $\sigma_{IG,n}^{cri}$. The mechanical behaviour of **IG Mode I** and **IG Mode II** fracturing are divided into two parts: (a) pre-peak linearity; and (b) post-peak softening. The fracture criterion of the intergranular fractures are

$$\text{IG Mode I:} \quad \begin{aligned} \sigma_{IG,n} \geq \sigma_{IG,n}^{cri} & \quad \partial\Omega_{IG}\mathbf{n} \Rightarrow \mathbf{f}_n = \mathbf{0} \quad \text{on } \partial\Omega_{IG}\mathbf{n} \\ |\sigma_{IG,t}| < \sigma_{IG,t}^{cri} & \quad \partial\Omega_{IG}\mathbf{n} \Rightarrow \mathbf{f}_t = \mathbf{0} \quad \text{on } \partial\Omega_{IG}\mathbf{t} \end{aligned} \quad (7.14)$$

$$\text{IG Mode II:} \quad \begin{aligned} \sigma_{IG,n} < \sigma_{IG,n}^{cri} & \quad \partial\Omega_{IG}\mathbf{t} \Rightarrow \mathbf{f}_n = c_n(\mathbf{u} \cdot \mathbf{n})\mathbf{n} \quad \text{on } \partial\Omega_{IG}\mathbf{n} \\ |\sigma_{IG,t}| \geq \sigma_{IG,t}^{cri} & \quad \partial\Omega_{IG}\mathbf{t} \Rightarrow \mathbf{f}_t = \mu_{IG,c}\mathbf{f}_n \quad \text{on } \partial\Omega_{IG}\mathbf{t} \end{aligned} \quad (7.15)$$

where $\sigma_{IG,t}^{cri}$ is the cohesive strength and $\mu_{IG,c}$ is the friction coefficient on grain boundaries. The transgranular contacts are element boundaries which behave as FPZ models as shown in Fig. 7.5. The mechanical behaviour of **TG Mode I** and **TG Mode II** fracturing are simplified as

$$\text{TG Mode I:} \quad \begin{aligned} d_n = 1.0 & \quad \partial\Omega_{TG}\mathbf{n} \Rightarrow \mathbf{f}_n = \mathbf{0} \quad \text{on } \partial\Omega_{TG}\mathbf{n} \\ |\mathbf{u}_n| \in [u_{r,n}, \infty] & \quad \partial\Omega_{TG}\mathbf{n} \Rightarrow \mathbf{f}_t = \mathbf{0} \quad \text{on } \partial\Omega_{TG}\mathbf{t} \end{aligned} \quad (7.16)$$

$$\text{TG Mode II:} \quad \begin{aligned} d_t = 1.0 & \quad \partial\Omega_{TG}\mathbf{t} \Rightarrow \mathbf{f}_n = c_n(\mathbf{u} \cdot \mathbf{n})\mathbf{n} \quad \text{on } \partial\Omega_{TG}\mathbf{n} \\ |\mathbf{u}_t| \in [u_{r,t}, \infty] & \quad \partial\Omega_{TG}\mathbf{t} \Rightarrow \mathbf{f}_t = \mu_{TG,c}\mathbf{f}_n \quad \text{on } \partial\Omega_{TG}\mathbf{t} \end{aligned} \quad (7.17)$$

The variable d in Eq (7.16) and (7.17) are damage value of the cohesive bond, which is expressed as

$$\begin{aligned} \dot{d}_n &= \frac{\mathbf{u}_n - \mathbf{u}_{p,n}}{\mathbf{u}_{r,n} - \mathbf{u}_{p,n}} & \mathbf{u}_n \in [\mathbf{u}_{p,n}, \mathbf{u}_{r,n}] \\ \dot{d}_t &= \frac{\mathbf{u}_t - \mathbf{u}_{p,t}}{\mathbf{u}_{r,t} - \mathbf{u}_{p,t}} & \mathbf{u}_t \in [\mathbf{u}_{p,t}, \mathbf{u}_{r,t}] \end{aligned} \quad (7.18)$$

$\mathbf{u}_{r,n}$ and $\mathbf{u}_{r,t}$ are residual displacements of the FPZ in normal and tangential directions. d is an internal variable of contact \mathcal{C}_{ij} , the value of d is determined as $d = \max(|\dot{d}_n|, |\dot{d}_t|)$, the relations between the residual displacements and energy dissipation rate are

$$\begin{aligned} G_{IC} &= \int_{u_{p,n}}^{u_{r,n}} \sigma_{TG,n} du_n \\ G_{IIC} &= \int_{u_{p,t}}^{u_{r,t}} (\sigma_{TG,t}(t) - \sigma_{t,r}) du_t \end{aligned} \quad (7.19)$$

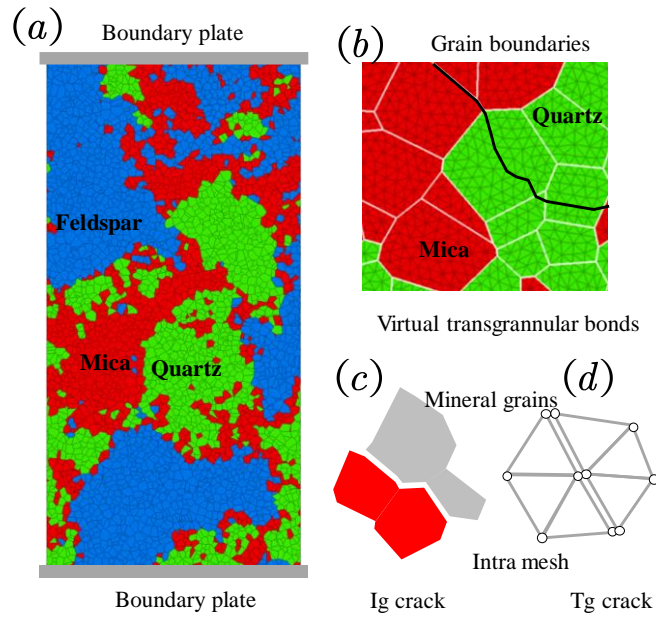


Fig. 7.5 The typical grain-based rock sample used to simulate granitic rock in GbCDM.

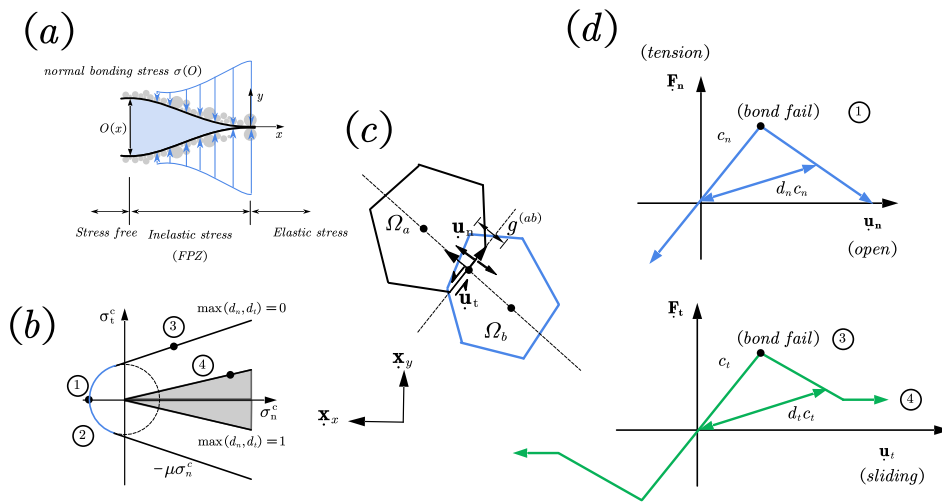


Fig. 7.6 Fracture models of inter and intra grains implemented in GbCDM.

7.4 Characterization on micro-parameters using nanoindentation

Most modeling practices consider microheterogeneity qualitatively and their choice of microparameters are

subjective. In this thesis, a novel approach to combine a detailed microscale characterization with modeling of heterogeneous geomaterials is presented. Microparameters, *e.g.*, grain size, mineral density, Young's modulus and poisson's ratio and fracture roughness are available from nanoindentation and scratch tests. The purpose of this method is to illustrate the actual microscopic heterogeneity combining established techniques and the accurate mechanical parameters are characterized by indentation tests (Fig. 7.7).

The nanoindentation results of Qtz, Fsp and ma for granite are shown in Fig. 7.8. Quartz (Qtz) has the largest elastic modulus and followed by feldspar as well as mica. The average elastic modulus of mica is 39 GPa, and that value of feldspar is 63 GPa. Quartz has the largest elastic modulus, about 108 GPa, the Poisson's ratios of the three minerals are 0.09, 0.26 and 0.3 respectively.

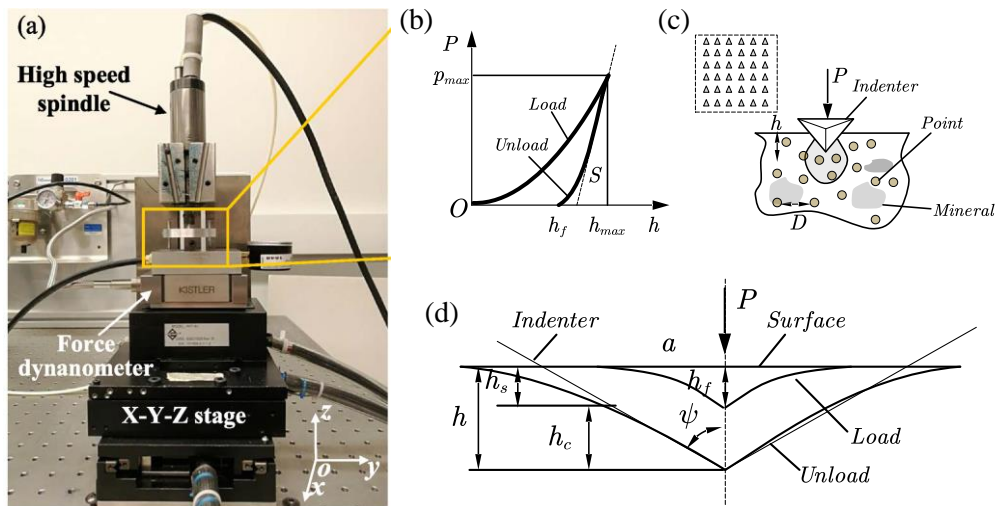


Fig. 7.7 (a) Experimental set-up of Nano Indenter. (b) Load-displacement curve of nanoindentation test, (c) grid indentation on a heterogeneous system, (d) main parameters of nano-indentation test.

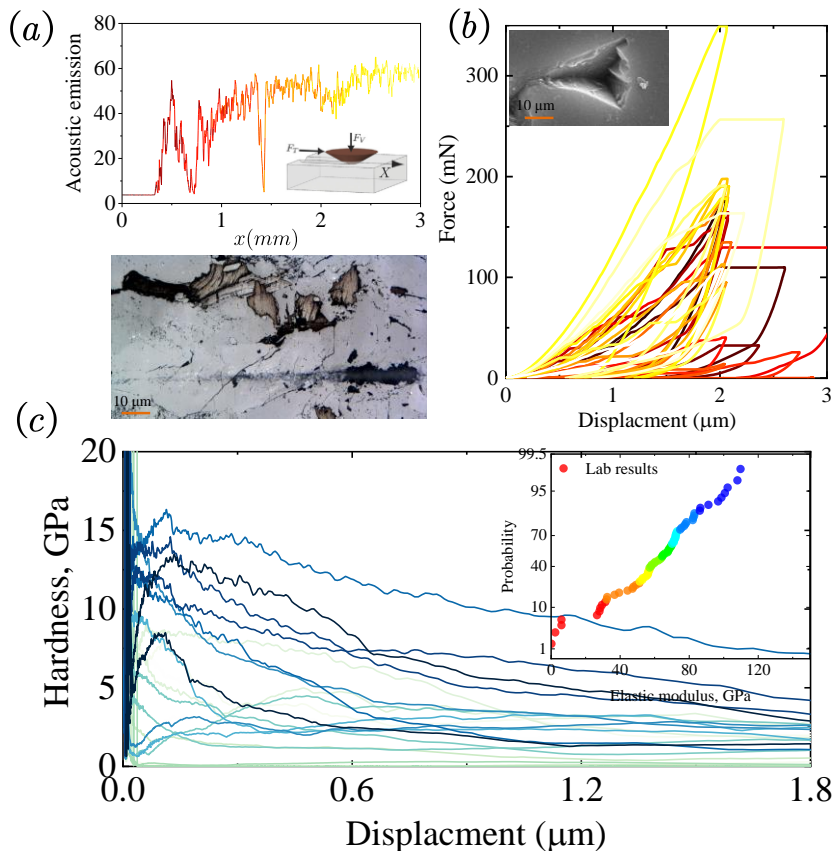


Fig. 7.8 Experimental results of nanoindentation on different mineral interfaces of granite.

8. The grain scale dynamic fracturing characteristics of heterogeneous rocks: insights from numerical modelling

8.1 Dynamic damage stress threshold

The crack initiation stress is identified according to the intensity of initiated cracks in the specimen. This stress threshold increases from 88.6 MPa to 123.4 MPa as the strain rate increases (Fig. 8.2 a and Table 8.1). Most microcracks generated at this moment are intergranular tensile cracks resulting from initial defects of mineral grains. Therefore, the Mode-I fracture toughness is commonly determined by the initially defected state of the sample and the sustainable capacity of the grain boundaries. The normalised crack initiation stress ranges from 0.38 to 0.52 with a roughly linear increasing, indicating that the crack initiation stress has less dependency on the strain rate in comparison with the peak strength. The crack damage stress is the point corresponding to the maximum crack strain which indicates the start of subsequently unstable fracturing. According to the microcracks distribution in Fig. 8.1, transgranular tensile cracks dominate the macrocracks coalescence, and in turn influence the stress threshold. Shear faults resulting from grain pulverization consume large strain energy, these faults also increase the friction sliding between grains. The macro failure transits from the splitting dominated fracturing to sliding dominated pulverization, which increases the σ_{cd} , and the range of σ_{cd}/σ_{dyn} is 0.82~0.95.

8.2 Criteria of pulverization and dynamic fragmentation

Fig. 8.3 shows that shear bands result in macro sliding between dominant fragments, and these bands are composed of transgranular and intergranular cracks clustering consuming considerable energy. Unloading induced macro tensile fracture (Fig. 8.3 b) successively breaks these dominant fragments into small debris, and the stored elastic strain energy is transformed into the kinetic energy of the fragments. This is the reason why the kinetic energy is dramatically increased when the strain rate is improved. Most microcracks appear in the direction parallel to wave propagation (Fig. 8.3 d), these cracks are dominated by transgranular tensile cracks which are far away from the shear bands. In general, these parallel cracks are the result of axial splitting induced by reflected tensile waves between grain boundaries. Another typical fracturing feature is the fracture network around the grains by intergranular tensile cracks as shown in Fig. 8.3 (e-f). These fractures are more likely to be generated by large grain rotations. More specifically, the macrocracks result from grain pulverization as shown in Fig. 8.3 g. These cracks are commonly existed on the shear bands and directly lead to the macro pulverization phenomenon. Apparently, this type of failure takes away most sliding energy but results in less residual kinetic energy.

The Class I only exists when the loading strain rate is low, and the unloading process is associated with huge elastic strain energy release. The failure state is characterised by a single fracturing or several fragments parallel to the loading direction. Class II is subjected to higher strain rate with all loss of cohesion. This catastrophic failure results in sample pulverization. In association with the dynamic mechanical classes, the fracturing patterns can be categorised into two main forms shown in Fig. 8.4 (a-j). The transition stages presented in Fig. 8.4 (f-i) show the successive inheritance from pattern I to pattern II. It can be concluded that: (a). Class I loading induces axial splitting fracturing adjacent to the free boundaries of the specimen as a result of micro tensile failure. This fracturing is coalesced to the main fracture surface and then results in the ultimate fragmentation. Since the fracturing toughness of intergranular contacts is much less than that of transgranular contacts, some branching cracks occur at the tip of the grain boundary. The lengths of these branching cracks are determined by the subsequent energy input. (b) Once the external energy is capable to drive the branching crack propagation, these secondary cracks nucleate into the fracture surface and localized fragments are generated. This fragmentation is a classical failure characterization of dynamic loading which consumes higher energy and in turns results in macro behaviours enhancement. (c) Once the external energy is high enough, the friction bands surrounding the fracture surface are induced by the large kinetic energy release of the particles. This kind of failure aims to transform the strain energy stored in the contacts to friction energy, which eventually leads to large deformation of the specimen.

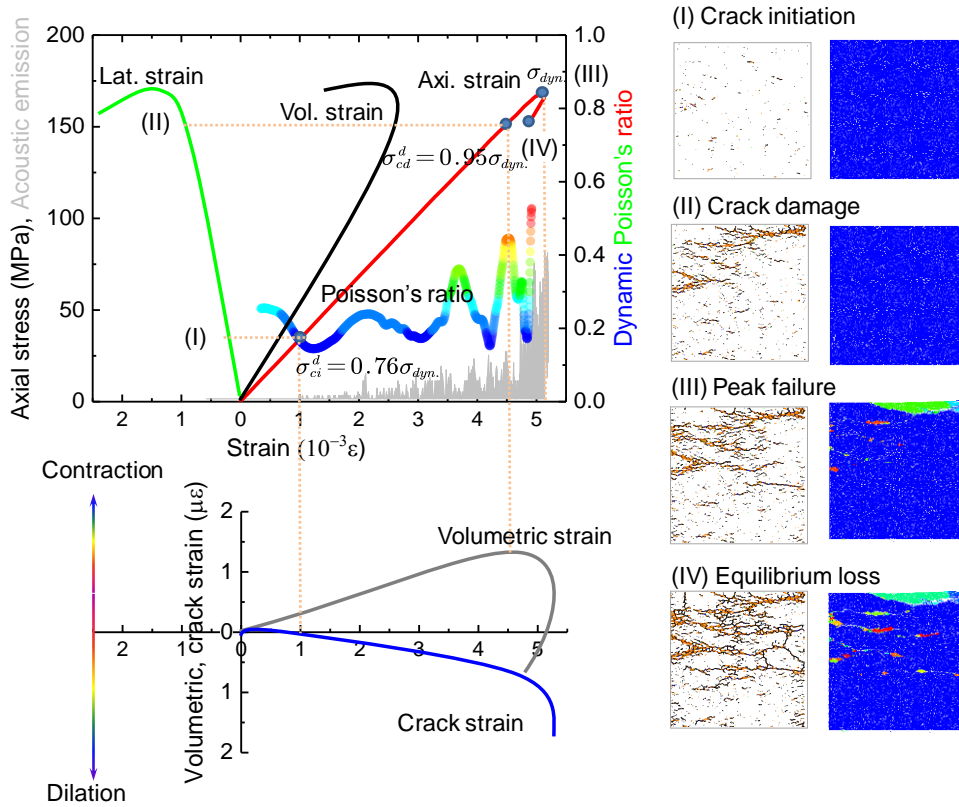


Fig. 8.1 Macro behaviour and micro-fracturing characteristic under different strain rates.

Table 8.1 Simulated results of granites at different strain rates

$\dot{\epsilon}$ (s^{-1})	Strength (MPa)			ω_d	DIF	Energy density (J/cm^2)			Crack area (mm^2)				
	σ_{ucs}	σ_{ci}	σ_{cd}			e_{dis}	e_{kin}	e_{fric}	IT	IS	TT	TS	
0.00001	129.6	66.3	117.3	0.14		0.86	0.06	0.80	61.79	3.72	55.61	4.13	
	47.6	168.2	88.6	159.79	0.19	1.30	1.89	0.69	1.39	75.08	3.35	50.72	1.18
	63.8	213.9	96.34	189	0.25	1.65	15.83	9.26	6.57	161.41	7.60	221.10	12.77
	102.7	247.8	104.36	203.78	0.305	1.91	27.50	18.06	9.49	186.28	8.06	298.86	22.12
	175.4	272.3	109.4	213.4	0.365	2.10	40.44	27.45	13.09	196.00	8.78	354.43	31.92
	196.4	292.4	116.4	238.7	0.394	2.26	51.44	35.68	15.83	213.12	9.12	422.20	41.61
	296.2	307.6	114.2	247	0.42	2.37	57.24	39.22	18.03	211.93	9.56	438.18	48.45
	334.2	319.2	123.4	260.5	0.54	2.46	68.91	48.36	20.62	223.37	9.42	476.46	56.64

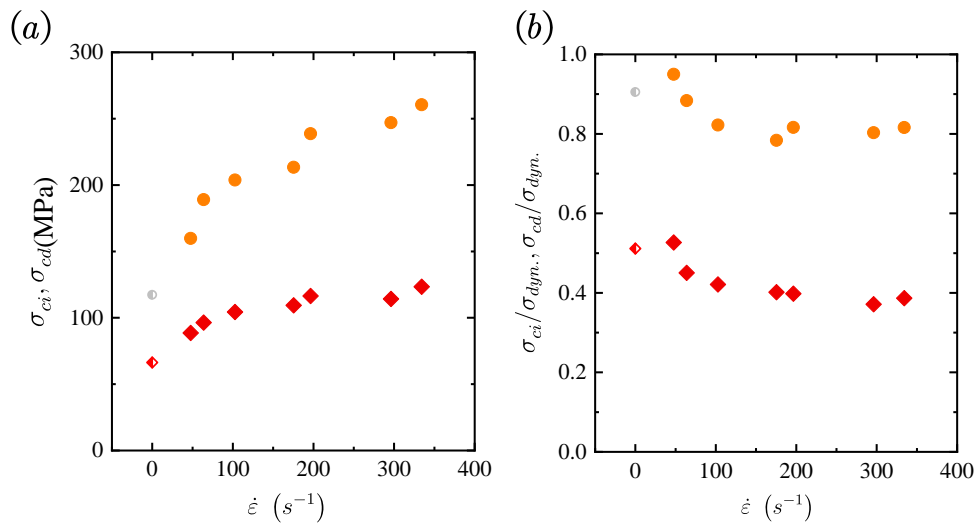


Fig. 8.2 (a) Stress threshold and (b) normalized stress thresholds as a function of strain rate.

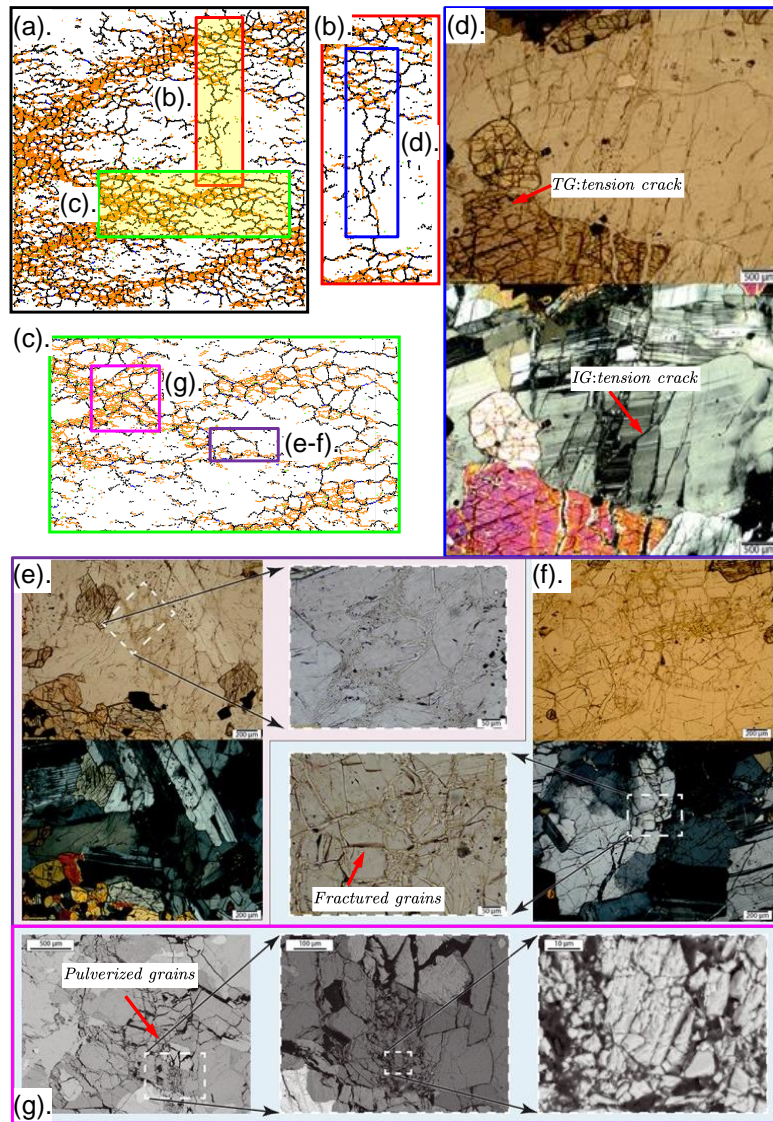


Fig. 8.3 (a) Micro cracks distribution of the specimen at an impact velocity 10 m/s and its comparison with relevant SEM scan results.

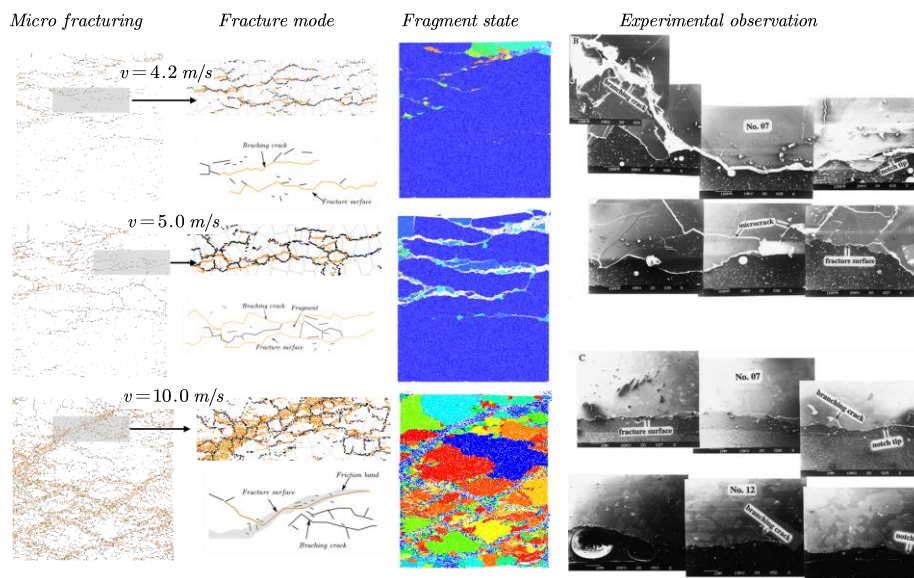


Fig. 8.4 Micro crack rupture difference at three different strain rates.

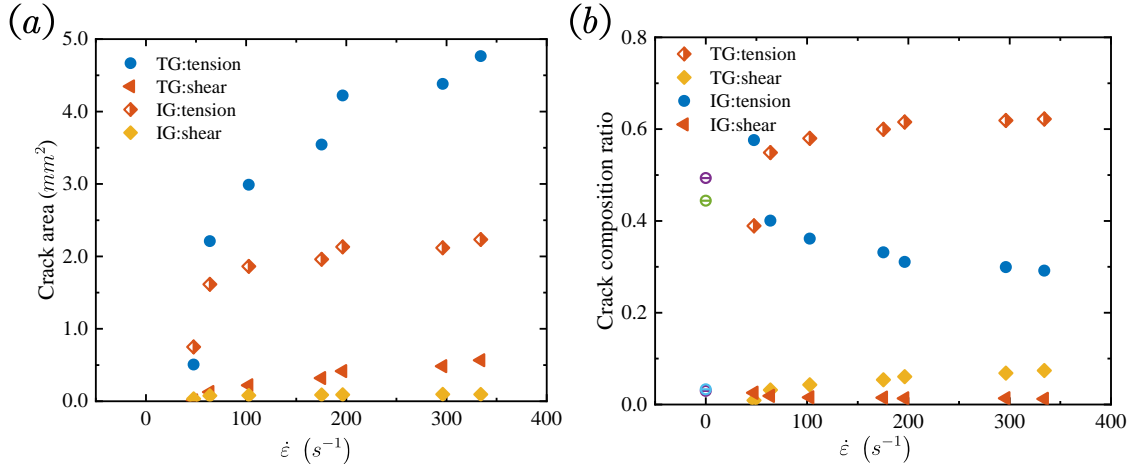


Fig. 8.5 Different crack types area and composition ratio with respect to various strain rates. (a) Crack area. (b) Crack composition ratio.

8.3 Microcracks fracturing transition

The fractured microcracks can be divided into Mode-I fracturing and Mode-II fracturing. According to the fractured properties, these cracks can be further classified as intergranular tensile cracks (IG: tension), intergranular shear cracks (IG: shear), transgranular tensile crack (TG: tension), and transgranular shear crack (TG: shear). It is widely accepted that grain boundary fracturing is the dominant failure in static test of brittle materials. These conclusions also can be observed in dynamic tests (Fig. 8.5). At low strain rates ($\dot{\epsilon} \leq 100 \text{ s}^{-1}$), especially for Class I loading, the intergranular tensile crack area has a dominant influence on the specimen fracturing with a composition ratio more than 57.6%. This value gradually decreases to 29.2% as the strain rate increases. Meanwhile, the transgranular tensile crack which resulted in grain pulverisation dramatically increases and shows a dominant composition at higher strain rate. Shear cracks (either intergranular or transgranular) seem to present similar behaviours, but the overall composition ratios are no more than 10%. From the transition of fracturing microcrack modes, it is agreed that the strain-rate dependency is related to the dominance of grain pulverisation.

8.4 Strain rate effects on transgranular fracturing

The intrinsic mechanisms governing the strain rate dependency for brittle materials are attributed to thermal activation, multiscale fracturing transition, energy dissipation dominated dynamic fragmentation and inertia effects. Fast crack propagation at an interface was investigated and the condition that cracks penetrate into minerals is

$$\frac{\mathcal{G}_{I_g}(v_1, \theta)}{\mathcal{G}_{T_g}(v_2)} > \frac{\mathcal{G}_{I_g,c}(v_1)}{\mathcal{G}_{T_g,c}(v_2)} \quad (8.1)$$

where $\mathcal{G}_{I_g,c}(v_1)$ and $\mathcal{G}_{T_g,c}(v_2)$ are the dynamic fracture toughness of the grain boundary and the mineral at crack velocities of v_1 and v_2 , respectively. $\mathcal{G}_{T_g}(v_2)$ and $\mathcal{G}_{I_g}(v_1, \theta)$ are the dynamic energy release rates when the crack deflects and penetrates, which are

$$\begin{aligned} \mathcal{G}_{I_g}(v_1, \theta) &= \frac{1-v^2}{E} [A_I(v_1) (k_I(v_1) K_{I_g,I}(\theta))^2 + A_{II}(v_1) (k_{II}(v_1) K_{I_g,II}(\theta))^2] \\ \mathcal{G}_{T_g}(v_2) &= \frac{1-v^2}{E} [A_I(v_2) (k_I(v_2) K_{T_g,I})^2] \end{aligned} \quad (8.2)$$

in which $K_{I_g,I}(\theta)$ and $K_{I_g,II}(\theta)$ are mode I and mode II stress intensity factors for the crack deflection on the grain boundary. The dynamic stress intensity factors can be derived according to static stress intensity factors by the universal function of crack speed v

$$\begin{aligned} k_I(v) &= \frac{1-v/c_R}{(1-v/c_p)^{1/2}} \\ k_{II}(v) &= \frac{1-v/c_R}{(1-v/c_s)^{1/2}} \end{aligned} \quad (8.3)$$

where c_s , c_p and c_R are the shear wave, dilatational wave and Rayleigh wave speeds in the solids and the other parameters $A_I(v)$ and $A_{II}(v)$ depending on the crack velocity v are

$$A_I(v) = \frac{v^2 \alpha_p}{(1-v)c_s^2 R(v)}$$

$$A_{II}(v) = \frac{v^2 \alpha_s}{(1-v)c_s^2 R(v)} \quad (8.4)$$

where $\alpha_p = \sqrt{1 - (v/c_p)^2}$, $\alpha_s = \sqrt{1 - (v/c_s)^2}$ and $R(v) = 4\alpha_s \alpha_p - (1 + \alpha_s^2)^2$. By substituting Eqs (8.2)-(8.4) to Eq (8.1), the energy release rate ratio for the transgranular fracturing can be expressed as

$$\frac{\mathcal{G}_{Ig}(v_1, \theta)}{\mathcal{G}_{Tg}(v_2)}$$

$$= \left(\frac{v_1}{v_2}\right)^2 \frac{R(v_2)}{R(v_1)} \frac{\alpha_p(v_1) k_I^2(v_1) \left(3 \cos \frac{\theta}{2} + \cos \frac{3\theta}{2}\right)^2 + \alpha_s(v_1) k_{II}^2(v_1) \left(\sin \frac{\theta}{2} + \sin \frac{3\theta}{2}\right)^2}{16\alpha_p(v_2) k_I^2(v_2)} \quad (8.5)$$

We note that Eq (8.5) vanishes when $v_1 = c_R$ and reaches its maximum for $v_1 = 0$. The measured crack velocity for mode I crack in laboratory will be no more than $0.5c_R$ (Ravi-Chandar and Knauss 1984), and at here, four cases $v_1 = 0.1c_R, 0.2c_R, 0.3c_R$ and $0.5c_R$ are studied and the transgranular crack velocity v_2 is set in a range from 0.1 to $2v_1$, as shown in Fig. 8.7. Therefore, the energy release rate ratio is a function of deflection angle θ and the transgranular crack velocity v_2 . For heterogeneous materials, the right-hand side part of Eq (8.1) spans a range from 0.25 to 0.5 as listed in Fig. 8.7. The crack velocities of crack deflection and crack penetration are not easy to measure in experiments. It is of interest to note that the interfacial crack velocity v_1 is larger than v_2 , without loss of simplicity, the change of v_2 ranges from 0.1 to 2.0 as shown in Fig. 8.7. For the case of $\mathcal{G}_{Ig,c}(v_1)/\mathcal{G}_{Tg,c}(v_2) = 0.5$, Ig fracturing will take place when the deflection angle is less than the critical angle, which is the focal point of two lines. Two types of micro fracturing are presented in Fig. 8.7 and the strain rate effect on the conversion of crack penetration can be summarized as:

- (i) The increase of interfacial crack velocity decreases the energy release rate ratio and results in a lower critical deflection angle dividing the Ig fracturing and Tg fracturing. That means more cracks will penetrate into minerals, which is confirmed by the results from simulations. Most Ig cracks fail in the lower angle range and the probability decreases as the deflection angle increases to 90° , which is perpendicular to the crack. Meanwhile, the increase of crack velocity leads to higher strain rate deformed in the solids and makes the microfracturing is rate dependent.
- (ii) For a set v_1 , the increase of crack velocity in minerals will shift the energy release rate ratio curve to up, which results in a higher deflection angle threshold to penetrate into minerals. From the experimental results reported by (Ravi-Chandar and Knauss 1984), the weak interface features higher interfacial velocity and the velocity ratio v_2/v_1 drops to zero for the strong grain boundary case when the deflection angle is beyond 68° .

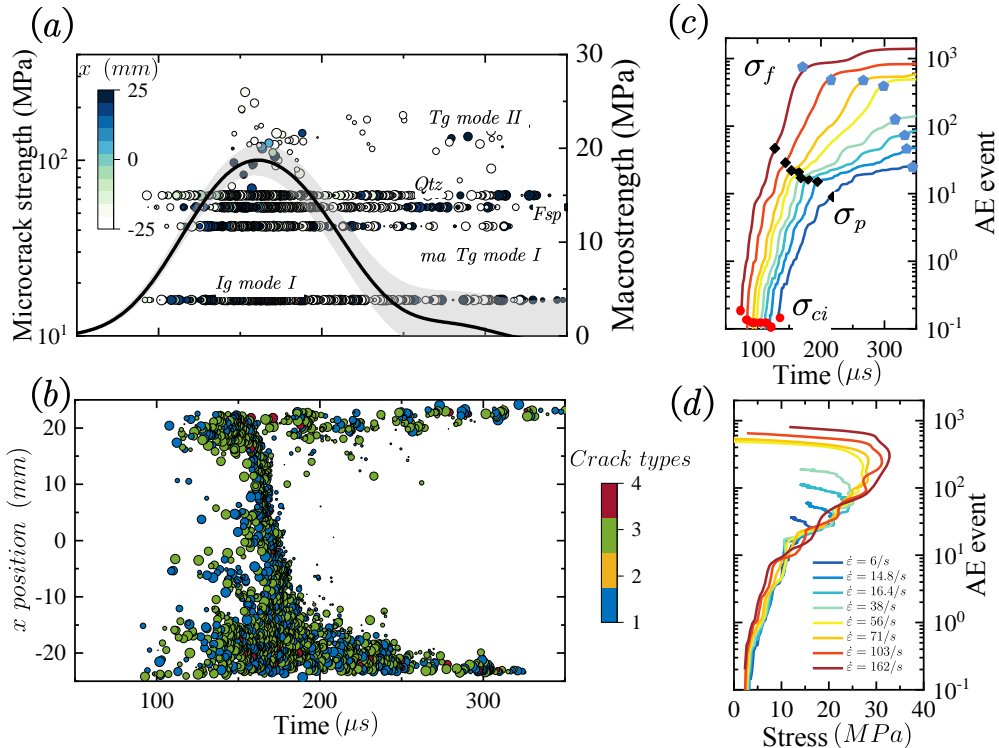


Fig. 8.6 (a) and (b) Typical fracturing patterns at the micro scale of Brazilian disc under dynamic loading. (c) and (d) Crack propagation and evolution under different impact velocities, the AE count as a function of time and stress.

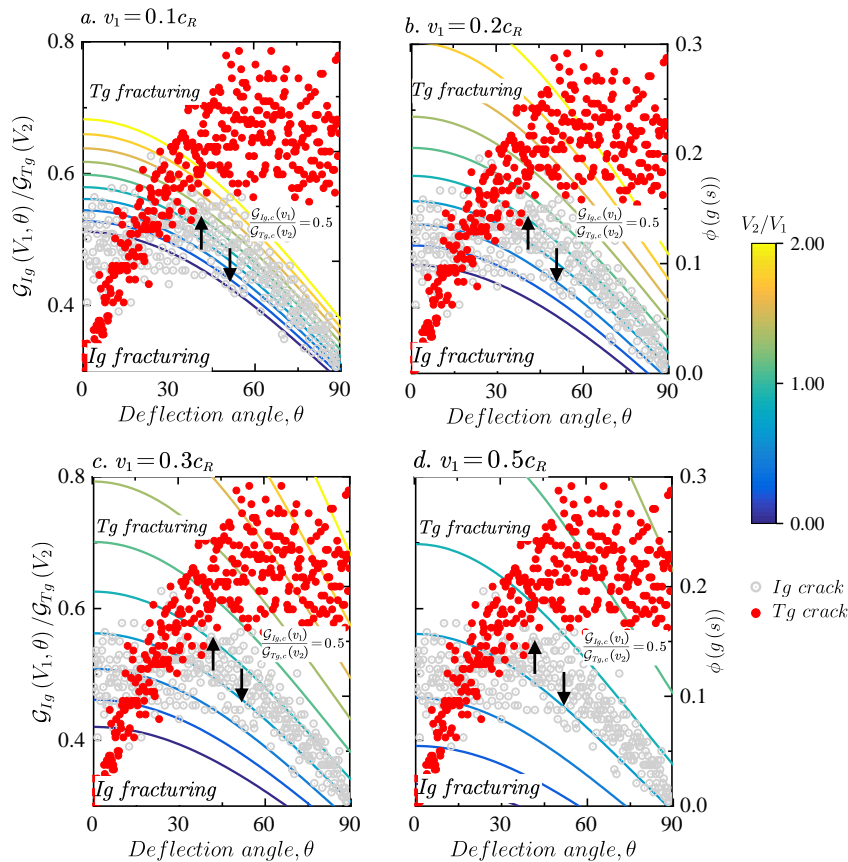


Fig. 8.7. The theoretical deflection angle as a function transgranular/intergranular energy release rate ratio at different crack velocities.

9. Protentional implications for rock engineering

- (9.1) The full-field deformation, crack initiation, crack velocity and failure sequence are explored to understand the actual dynamic tensile mechanics of rocks in cooperation with DIC technique. The accurate characterization of the dynamic tensile behaviours for rocks is of significance important in the area of rock bursts, blasting and mining (Chapter 4.1-4.2).
- (9.2) Two competitive mechanisms codetermine the rate dependency of surface roughness in dynamic fracturing. (i) Fast crack velocity leads to the departure of crack from its original tip and causes an increase in fractal dimension in forms of mists, hackles and microsteps. (ii) The transform to transgranular fracturing resulting in smoother surfaces decreases the fractal property. This result can be used to explain the underlying mechanism of dynamic crack branching, fractal fracturing as well as dynamic fragmentation (Chapter 4.3).
- (9.3) The process of dynamic fragmentation in rocks is reproduced and two kinds of dynamic failure patterns are presented. The results are applicable for explaining the age-old question why does some faults slip slowly, while others generate catastrophic ruptures, asymmetric faulting, and grain-scale pulverization due to high strain rate loads (Chapter 5.1-5.2).
- (9.4) Statistical distributions are compared with experimental results and a novel energy-based fragment model is proposed. The contribution of predictive capabilities to dynamic fragmentation of brittle solids can be used to estimate the fragment size in many engineering applications *e.g.*, rockfalls, mineral processing, blasting and planetary collision (Chapter 5.3).
- (9.5) The random fractured rock model with multiple cracks considering the effect of crack velocity is built to derive the unified dynamic strength model. The recommended values for the characteristic strain rate and strain rate increase factor of different rocks are performed. This is the first model describing the dynamic strength from theoretical analysis and the physical meanings of the two parameters are explained. It provides unbiased

references to the engineering applications regarding the fact that present investigations or reports are often estimated by trail and error (Chapter 6).

- (9.6) The newly developed mGbCDM has the ability to mimic the grain-scale fracturing initiation, propagation, interaction and coalescence inter or intra-mineral grains in heterogeneous rocks at laboratory scale. This software is also applicable for site-scale modelling *e.g.*, landslides, underground excavation, oil/gas recovery and rock mass stability, considering the actual failure of rocks. Moreover, the developed software, relevant results and associated input-files will be made **publicly available** (Chapter 7).
- (9.7) The explicit consideration of the actual microheterogeneity in rocks both *in-situ* and in the laboratory is performed to build the bridge linking the variability of microstructures with the macro dynamic properties which shows significant rate dependency, including (a) what's the actual heterogeneity on grain scale and how to characterize it in modelling? (b) how to develop the relation between the micro properties and macro behaviours? and (c) what's reason causes the conversion from intergranular fracturing to transgranular fracturing in solids? Due to the difficulty of reproduction the natural earthquake in the laboratory, the available computational method can be used to model the site-scale faulting will rather desirable (Chapter 8.1-8.3).
- (9.8) The conversion of microscopic failure from intergranular fracturing to transgranular fracturing is the underlying mechanism leading to strain rate dependency of rocks. The percentage of transgranular fracturing increases from 37% to 64% as the strain rate increases. The results provide useful references for understanding the intrinsic mechanism of strain rate and dynamic fracturing (Chapter 8.4).

Selected references

- Aydan (2016) Large rock slope failures induced by recent earthquakes. *Rock Mech Rock Eng* 49:2503–2524
- Cereceda D, Graham-Brady L, Daphalapurkar N (2017) Modeling dynamic fragmentation of heterogeneous brittle materials. *Int J Impact Eng* 99:85–101
- Cho N, Martin CD, Sego DC (2007) A clumped particle model for rock. *Int J Rock Mech Min Sci* 44:997–1010
- Cintala MJ, Berthoud L, Hörz F (1999) Ejection-velocity distributions from impacts into coarse-grained sand. *Meteorit Planet Sci* 34:605–623
- Dekhoda S, Hood M (2013) An experimental study of surface and sub-surface damage in pulsed water-jet breakage of rocks. *Int J Rock Mech Min Sci* 63:138–147
- Doan ML, Gary G (2009) Rock pulverization at high strain rate near the San Andreas fault. *Nat Geosci* 2:709–712
- Dor O, Ben-Zion Y, Rockwell TK, Brune J (2006) Pulverized rocks in the Mojave section of the San Andreas Fault Zone. *Earth Planet Sci Lett* 245:642–654
- Dor O, Yildirim C, Rockwell TK, et al (2008) Geological and geomorphologic asymmetry across the rupture zones of the 1943 and 1944 earthquakes on the North Anatolian Fault: Possible signals for preferred earthquake propagation direction. *Geophys J Int* 173:483–504
- Feng XT, Liu J, Chen B, et al (2017) Monitoring, Warning, and Control of Rockburst in Deep Metal Mines. *Engineering* 3:538–545
- Glenn LA, Chudnovsky A (1986) Strain-energy effects on dynamic fragmentation. *J Appl Phys* 59:1379–1380
- Grady DE (1982) Local inertial effects in dynamic fragmentation. *J Appl Phys* 53:322–325
- Hajiabdolmajid V, Kaiser P (2002) Brittleness of rock and stability assessment in hard rock tunneling. *Tunn Undergr Sp Technol* 18:35–48
- Heuzé FE (1990) An overview of projectile penetration into geological materials, with emphasis on rocks. *Int J Rock Mech Min Sci Geomech Abstr* 27:1–14
- Kim K, Bolander JE, Lim YM (2013) Failure simulation of RC structures under highly dynamic conditions using random lattice models. *Comput Struct* 125:127–136
- Kolsky H (1949) An investigation of the mechanical properties of materials at very high rates of loading. *Proc Phys Soc Sect B* 62:676–700
- Li XF, Zhang QB, Li HB, Zhao J (2018) Grain-Based Discrete Element Method (GB-DEM) Modelling of Multi-scale Fracturing in Rocks Under Dynamic Loading. *Rock Mech Rock Eng* 51:3785–3817
- Miller O, Freund LB, Needleman A (1999) Modeling and simulation of dynamic fragmentation in brittle materials. *Int J Fract* 96:101–125
- Mitchell TM, Ben-Zion Y, Shimamoto T (2011) Pulverized fault rocks and damage asymmetry along the Arima-Takatsuki Tectonic Line, Japan. *Earth Planet Sci Lett* 308:284–297
- Naimark OB, Uvarov S V., Davydova MM, Bannikova IA (2017) Multiscale statistical laws of dynamic fragmentation. *Phys Mesomech* 20:90–101
- Nemat-Nasser S, Horii H (1982) Compression-induced nonplanar crack extension with application to splitting, exfoliation, and rockburst. *J Geophys Res* 87:6805–6821
- Ravi-Chandar K, Knauss WG (1984) An experimental investigation into dynamic fracture: IV. On the interaction of

- stress waves with propagating cracks. *Int J Fract* 26:189–200
- Sanchidrián JA, Segarra P, López LM (2007) Energy components in rock blasting. *Int J Rock Mech Min Sci* 44:130–147
- Vagnon F, Ferrero AM, Alejano LR (2020) Reliability-based design for debris flow barriers. *Landslides* 17:49–59
- Yew CH, Taylor PA (1994) A thermodynamic theory of dynamic fragmentation. *Int J Impact Eng* 15:385–394
- Zhang QB, Zhao J (2014) A review of dynamic experimental techniques and mechanical behaviour of rock materials. *Rock Mech. Rock Eng.* 47:1411–1478
- Zhang Z (2017) Kinetic energy and its applications in mining engineering. *Int J Min Sci Technol* 27:237–244
- Zhou YX, Xia K, Li XB, et al (2012) Suggested methods for determining the dynamic strength parameters and mode-I fracture toughness of rock materials. *Int J Rock Mech Min Sci* 49:105–112